FABRICATION OF HIGHLY CONDUCTIVE AND FLEXIBLE HYBRID CARBON

NANOFILMS: 1D CARBON NANOTUBES MEET 2D GRAPHENE

by

MIN JEONG

Graduate School-Newark

Rutgers, The State University of New Jersey

in partial fulfillment of the requirements

for the degree of

Master of Science

Graduate Program in Chemistry

written under the direction of

Dr. Huixin He

and approved by

‾‾‾‾‾‾‾‾‾‾‾‾‾‾‾‾‾‾‾‾‾‾‾‾

‾‾‾‾‾‾‾‾‾‾‾‾‾‾‾‾‾‾‾‾‾‾‾‾

‾‾‾‾‾‾‾‾‾‾‾‾‾‾‾‾‾‾‾‾‾‾‾‾

Newark, New Jersey

May, 2012

ABSTRACT OF THE THESIS

FABRICATION OF HIGHLY CONDUCTIVE AND FLEXIBLE HYBRID CARBON

NANOFILMS: 1D CARBON NANOTUBES MEET 2D GRAPHENE

By MIN JEONG

Thesis Director:

Dr. Huixin He

Carbon nanotubes (CNTs) and graphene are the two most conductive members among carbon nanomaterials. For industrial applications, these nanomaterials are attracting great attention for fabrication of flexible conducting films. However, the electronic performance of either CNT or graphene film has yet to reach their theoretical expectations due to high resistance and tunneling/Schottky barriers at the junctions between nanotubes or between graphene sheets. One of the important observations was that CNTs and graphene sheets can be crosslinked during and/or after film fabrication, which largely decrease inter-tube or inter-sheet resistance. However, the current solution-processing techniques for the film fabrication, such as spin coating, layer-by-layer assembly, and vacuum filtration have disadvantages and limitations. In this thesis, we developed an efficient film assembly approach as well as a facile transfer process.

The first chapter of this thesis provides an overview on structure and properties of CNTs and graphene.

In the second chapter, we used our newly developed microwave-enabled dispersion technique to synthesize highly conductive dispersible CNTs and graphene with low-density of oxygen-containing groups, without a need of surfactant/stabilizer. As we fabricated Microwave-enabled low-oxygen multi-walled nanotube only (ME-LOMWNT-only), Microwave-enabled low-oxygen graphene only (ME-LOGr-only), and ME-LOMWNT/ME-LOGr hybrid films using vacuum filtration, we found that the hybrid films are highly conductive relative to either the ME-LOMWNT-only or ME-LOGr-only film. The conductivity of the hybrid films depends on their composition, where a weight ratio of 97/3 between MWNTs and graphene reached the highest conductivity of 247,812 S m^{-1}, which is two times higher than those of SWNT/graphene hybrid films reported by Coleman et al.[8] In this work, we found crosslinks between MWNTs and graphene, which could be further promoted in acidic environment. These crosslinks between MWCNT and graphene enhanced the film conductivity.

The aim of the third chapter was to fabricate high quality graphene films and MWNT/graphene hybrid films using interfacial self-assembly approach. We observed the different assembly behavior of ME-LOMWNT and ME-LOGr due to their different shape and surface energy. Then, we optimized the parameters to fabricate high quality of ME-LOMWNT/ME-LOGr hybrid films. Moreover, we developed an efficient approach to transfer the self-assembled film at this water/oil interface onto substrates for future electrical characterization and device fabrications.

Table of Contents

Table of Figures

x

List of Tables

CHAPTER 1   Introduction

1.1   Carbon-based materials

Carbon is one of the most abundant elements in nature, which is capable of forming compounds with diverse orbital hybridizations such as sp, sp^2, and sp^3. In nanoscience, the sp^2 hybridized carbon system is the subject of much attention among the possible orbital hybridizations of carbon due to its capability of forming different architectures with various chemical and physical properties. With the discovery of C_{60} Buckminsterfullerene, a cage-like carbon molecule, in 1985 (Fig. 1a), a new allotrope of carbon was introduced.[1,2,3] This discovery greatly stimulated the creativity and synthesis of novel nanoscale crystalline carbon forms. Over the past few decades, carbon-based nanomaterials with various allotropes exhibiting each possible dimensionality have been revealed.[4,5,6,7,8] Examples are fullerene molecules (0D) (Fig 1.1a), nanotubes (Fig 1.1b) and graphene ribbons (1D) (Fig 1.1c), graphene sheets (2D) (Fig 1.1d), and graphite (3D) (Fig 1.1e). Owing to the extraordinary versatility of dimensionality and structure, each nanomaterial has its unique optical, electrical, mechanical, and thermal properties. With their unique and novel properties, carbon-based materials are powerful prospects of materials science and condensed-matter physics.
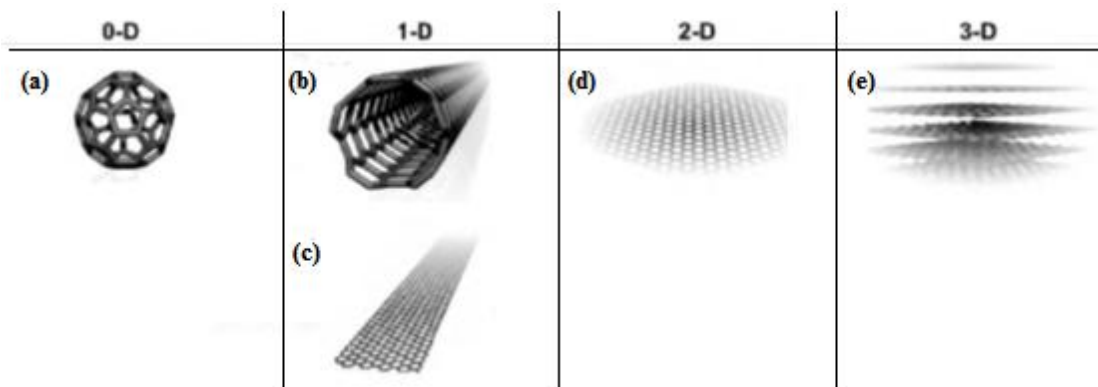
Fig 1.1 Schematic illustrations of sp^2-like hybridized carbon nanostructures of different dimensionalities, 0D, 1D, 2D, and 3D: (a) C$_{60}$: Buckminsterfullerene; (b) carbon nanotube; (c) graphene nanoribbons; (d) graphene surface; (e) 3D graphite crystal. Reproduced from *Nano Today 5.* **2010**, 352.

1.2   Graphene

Graphene is a two-dimensional single layer consisting of sp^2 hybridized carbon atoms in a perfect hexagonally honeycomb lattice.[9] Among the variety of carbon nanomaterials, graphene is the first material that has been isolated in sufficient quantity from the environment to be considered freestanding which is receiving tremendous interest.[10,11] In addition, graphene has recently arisen as a novel carbon allotrope for a range of potential applications because of its giant intrinsic charge mobility, incredible thermal and electrical conductivity, and superior mechanical strength.[12,13,14,15,16,17] Graphene also has acted as an ideal two-dimensional building block to describe and predict the formation and properties of other carbon-based nanomaterials, including graphite, nanotubes, ribbons, and fullerenes.[18] Additionally, graphene has unexpected reactivity with hydrogen to form graphane, a fully hydrogenated graphene sheet, that can be used as insulator, for hydrogen storage, or in astrochemistry.[19]
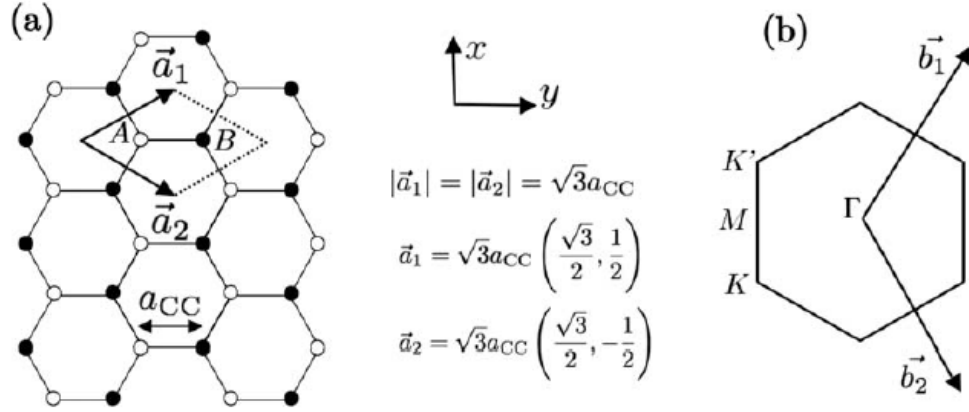
Fig 1.2 Schematic illustrations of: (a)basis vectors in the hexagonal lattice of graphene and (b)the corresponding Brillouin zone. Reproduced from *Eur. Phys. J. B.* **2009**.

In the reported work of Charlier and co-workers, the electronic properties of graphene are well described.[20] The crystal structure of a single layer graphene sheet with typical thickness of approximately 0.4 nm has a unique electronic structure, a zero band-gap. In a hexagonal lattice, there are two atoms per unit cell (A and B) with basis vectors $\vec{a_1}$ and $\vec{a_2}$ (Fig 1.2a), which form two A-B sub-lattices. When electrons are migrating between these two A-B sub-lattices, the graphene π and π* electronic energy bands that are symmetric with respect to the valence and conduction bands are formed, which intersect at Dirac points, K and K' (Fig 1.3). Linear electronic band dispersion that formed near the Dirac point results in zero effective mass excitons called Fermions, which can be described by the Dirac equation. The energy dispersion relation at low energies near the Dirac is represented in the following equation:

$$E\big(k_x, k_y\big) = \pm\gamma_0\sqrt{1 + 4\cos\left(\frac{\sqrt{3}k_x a}{2}\right)\cos\left(\frac{k_y a}{2}\right) + 4\cos^2\left(\frac{k_y a}{2}\right)} \qquad (1.1)$$

where k_x and k_y are wavevectors, γ_0 is a transfer integral, and a is the lattice constant.

The electronic states of these Fermions show an unusual property of being not influenced by external sources of elastic disorder, which lead to the intrinsic electrical mobility of graphene sheets, as large as 10^5 cm^2 V^{-1} s^{-1}.[10]
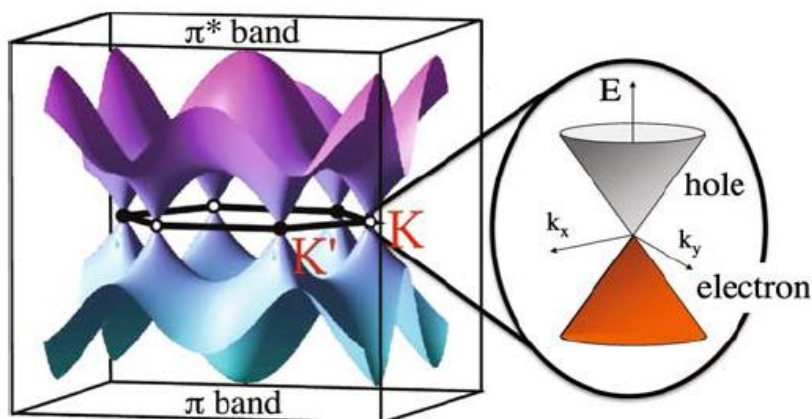
Fig 1.3 Schematic illustration of graphene π and $\pi*$ electronic energy symmetric bands with respect to the valence and conduction bands., intersecting at Dirac points K and K'. Reproduced from *Eur. Phys. J. B.* **2009**, 4.

Balandin and co-workers have reported the thermal conductivity of a suspended graphene sheet obtained by mechanical exfoliation as being between $(4.84 \pm 0.44) \times 10^3$ and $(5.30 \pm 0.48) \times 10^3$ W m^{-1} K^{-1}.[21] However, in a more recent measurement of chemical vapor deposition (CVD)-grown suspended graphene, a lower value of approximately 2.5×10^3 W m^{-1} K^{-1} has been measured.[22] Yet, this value is still superior to experimental values for carbon nanotubes and diamond.

Graphene is considered as one of the strongest materials ever tested. The breaking strength of graphene (Young's modulus of ca. 1 TeraPascal) is about 5 times larger than that of steel.[23] Using atomic force microscope (AFM), a Young's modulus was determined as 0.5 TPa.[24] These two reported values are different because the measurement varies with the number and the defect types present within the graphene

sheet. Despite the defects within the sheet, graphene is still considered very strong and rigid. Graphene, with such a high mechanical strength, is promising for applications such as pressure sensors and resonators.[24]

With such outstanding electrical, thermal, and mechanical properties, interest in graphene has dramatically increased. And, as mentioned previously, graphene is considered as an ideal building block for other carbon-based nanomaterials, such as carbon nanotubes.

1.3   Carbon nanotubes

As the two-dimensional graphene is rolled up into a cylindrical structure, it forms one-dimensional carbon nanotubes (CNTs). They were first discovered and characterized by Iijima in 1991.[7] Since the in discovery, carbon nanotubes have received a great deal of attention due to their unique properties, including excellent electron transfer, mechanical flexibility, thermal stability, and a high aspect ratio.[25] A conceptual view of a carbon nanotube is considered as a hexagonal lattice of carbon rolled up into a hollow cylinder. The different combinations of the rolling angle and radius lead to different structures and properties of carbon nanotubes.[26] Fundamentally, carbon nanotubes are categorized into two types (Fig 1.4): (1) single-walled nanotubes (SWNTs), and (2) multi-walled nanotubes (MWNTs).
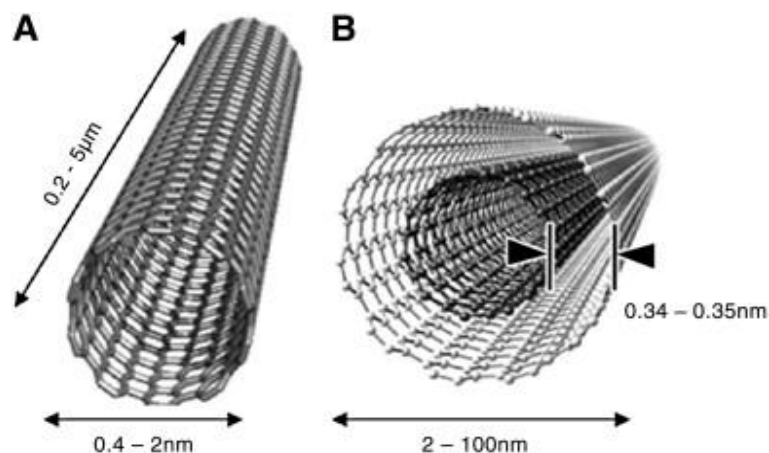
Fig 1.4 (a)single-walled nanotube (SWNT) and (b)multi-walled nanotube (MWNT). Reproduced from *J. Nucl. Med.*, **2007**, 48(7), 1040.

Single-walled nanotubes are made by seamlessly rolling up a single layer of graphene into a hollow cylinder of uniform diameter with a varied tube length.[28] Multiwalled nanotubes are in coaxial cylindrical structure, consisting of multiple layers with an interlayer spacing of 0.34nm, which is close to the spacing distance of graphite.[27]
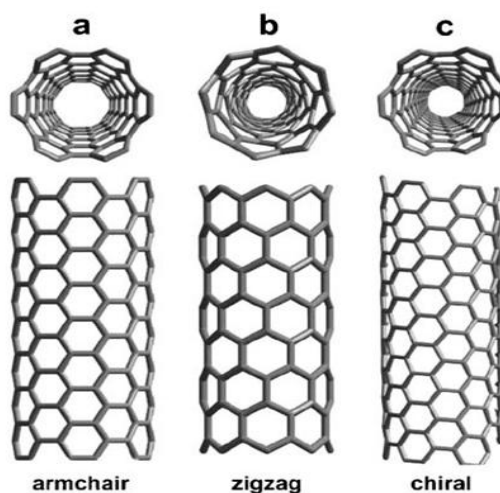
Fig 1.5 Classifications of carbon nanotubes.(a) armchair, (b) zigzag, and (c) chiral nanotubes. Reproduced from *Mater. Sci. and Engineering B* **2005**, 119, 105.
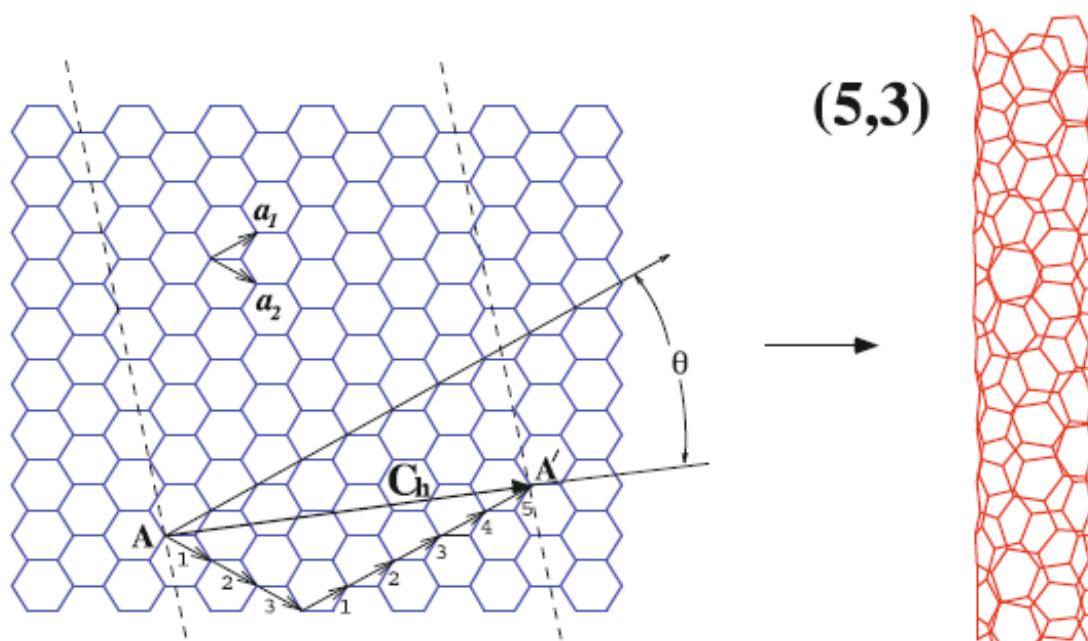
Fig 1.6 Schematic illustration of graphene (blue) being rolled up into cylinder structure carbon nanotube (red). A possible way of forming (5,3) zigzag nanotube is shown, by joining two crystallographically equivalent sites (A and A') on a graphene sheet by the chiral vector (C_h). Reproduced from *Eur. Phys. J. B.* **2009**, 11.

The different rolling angles produce different classifications of nanotubes: armchair, zigzag, or chiral nanotubes (Fig 1.5). In work of Dubois et al., they have presented how a 2D graphene sheet structurally forms into a 1D carbon nanotube.[20] The type of nanotubes can be specified in terms of the graphene lattice vectors. Fig 1.6 displays a possible way to form a nanotube by rolling up the graphene into a cylinder structure. Two crystallographically equivalent sites (A and A') on a graphene sheet are joined by the chiral vector (C_h), which represents a possible pathway of rolling up the graphene sheet.[28] The relative position of the chiral vector ($C_h = na_1 + ma_2$) can be denoted by a pair of indices (n, m) and unit vectors of the graphene lattice (a_1 and a_2).

Because this chiral vector defines the circumference of the nanotube, the diameter of the

nanotube (d_t) can be calculated with an equation:

$$d_t = \frac{|C_h|}{\pi} = \frac{a}{\pi}\sqrt{n^2 + nm + m^2} \qquad (1.3)$$

where a is the lattice constant. The chiral angle of the tube (θ), which is the angle

between C_h and a_1, can be estimated.

$$cos\theta = \frac{C_h \cdot a_1}{|C_h||a_1|} = \frac{(2n+m)}{(2\sqrt{n^2+nm+m^2})} \qquad (1.4)$$

This chiral angle is in the range of,$0° \leq |\theta| \leq 30°$, and indicates the tilt angle of the

hexagons with respect to the direction of the nanotube axis.
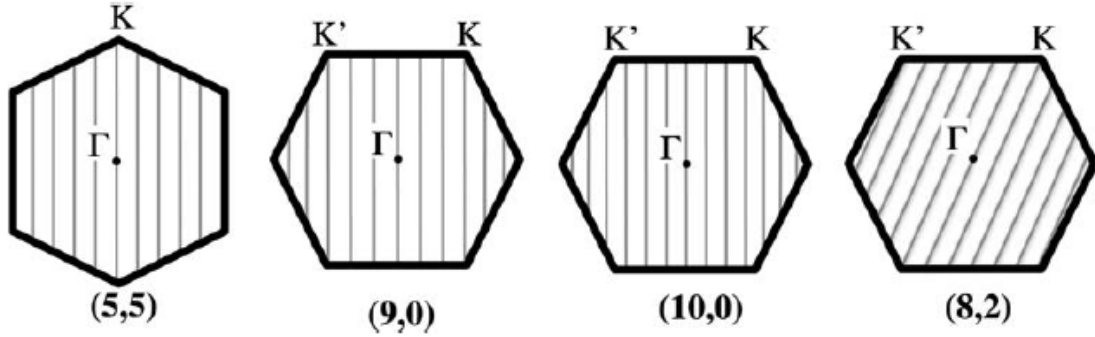
Fig 1.7 Nanotubes with allowed k-vectors. (5,5) armchair; (9,0) and (10,0) zigzag; and (8,2) chiral nanotubes. Reproduced from *Eur. Phys. J. B.* **2009**, 12.

Zigzag and armchair nanotubes are two types of achiral nanotubes. Zigzag nanotubes

have the chiral angle at 0° with chiral indices (n,0), where m=0. Carbon-carbon bonds of

this type of nanotubes are parallel to the nanotube axis, exhibiting a zigzag pattern along

the circumference. In contrast, armchair nanotubes have the chiral angle at 30° with the

indices (n,n), where n=m. For armchair tubes, carbon-carbon bonds are perpendicular to

the nanotube axis that they form an armchair pattern along the circumference. Unlike the

two types of achiral nanotubes, chiral nanotubes have indices, where n,m≠n≠0. Due to

the periodic boundary conditions imposed in the circumferential direction, only allowed

k-vectors around the nanotube circumference are quantized (Fig 1.7).

The key factor that determines the electronic properties of carbon nanotubes is

their chiral vector, C_h = (n,m), because it determines the helicity and tube diameter, which

influence the energy band gap of the nanotubes.[20] Generally, if n-m = 3ℓ, where ℓ is an

integer, then the corresponding carbon nanotube is considered as a metal; otherwise, it is

a semiconductor.
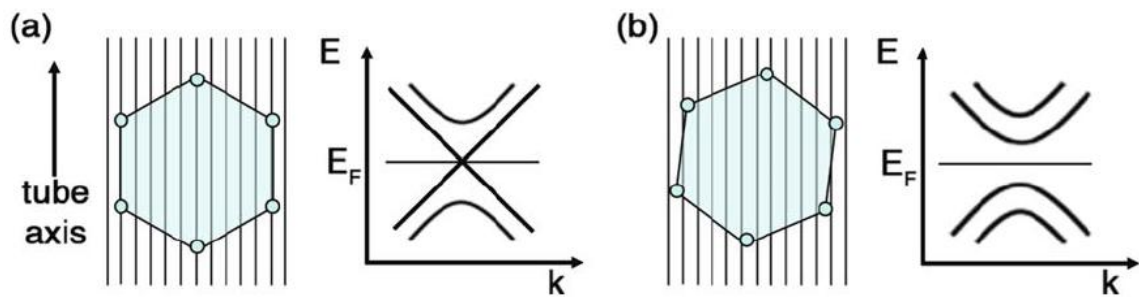
Fig 1.8 (a) Metallic nanotube, showing linear dispersion relation; (b) Semiconducting nanotube, showing energy gap . Reproduced from *Eur. Phys. J. B.* **2009**, 12.

All the armchair and the subset of (n,0) zigzag nanotubes satisfy the condition

with n-m = 3ℓ, which makes them to have metallic property.[29,30] The allowed k-vectors of

these metallic nanotubes include the K point of the graphene Brillouin zone, and they

present a linear energy-momentum relation close to the Fermi level, E_F (Fig 1.8a).[31] These

metallic nanotubes carry an electric current density of 4×10^9 A/cm^2, which is more than

thousands times greater than that of copper.[32]

On the other hand, carbon nanotubes with a condition n-m = $3\ell \pm 1$ represents a semiconducting behavior. For the semiconducting nanotubes, the K point on the graphene Brillouin zone is not an allowed vector, which shows an energy gap (Fig 1.8b) with estimated value of:

$$\Delta E_g^1 = \frac{2\pi a \gamma_0}{\sqrt{3}|C_h|} = \frac{2a_{cc}\gamma_0}{d_t} \tag{1.5}$$

As it was briefly mentioned before, the chiral vector also determines the tube diameter, which also influences the electric property of the nanotubes. Following the equation above, the energy gap decreases with the inverse of the tube diameter d_t ($d_t = |C_h|/\pi$). Since the energy gap is inversely proportional to the tube diameter, a semiconducting nanotube with very small energy-gap would have a very large diameter.[20]

Although the theoretical carbon nanotubes possess these amazing intrinsic electrical, mechanical, and thermal properties, in reality, these properties are limited by defects in synthesized carbon nanotubes.[33,34,35,36,37,38,39,40,41,42] To deal with that problem, high-temperature thermal annealing has been widely used to reduce the defects on the nanotubes.[43] However, this process is inefficient due to its cost and time requirement.

Fortunately, there has been a finding that carbon nanotubes have strong microwave absorption.[44,45,46] Microwave irradiation has been used to anneal CNTs,[47] which showed great improvement in mechanical and electrical properties.

1.4   Microwave chemistry

In the past decades, microwave-assisted reactions attracted great attention in nanostructure chemistry due to the strong microwave absorption of carbon nanostructures.[44,48] Many microwave-assisted studies have already been performed on

carbon materials, such as fullerenes,[49] carbon nanotubes,[50,51,52,53] and carbon nanohorns.[54] Compared to conventional heating, microwave-assisted chemistry often lowers reaction time, increases yield while reducing side reactions, and thus produces cleaner products.[55]
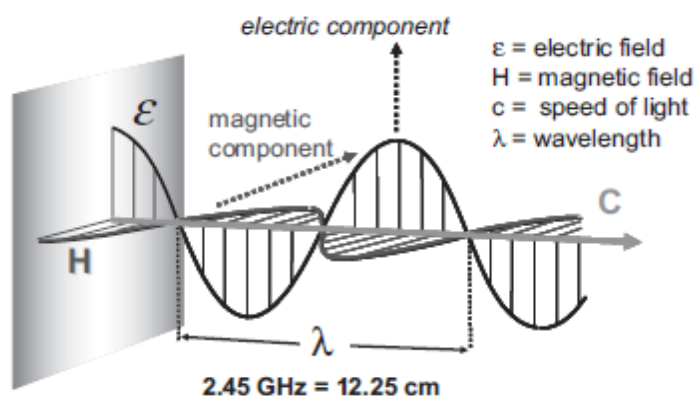
Fig 1.9 Microwave irradiation wave, showing electric and magnetic components. Reproduced from Practical Microwave Synthesis of Organic Chemists. *Wiley-VCH, Weinheim*, **2009**.
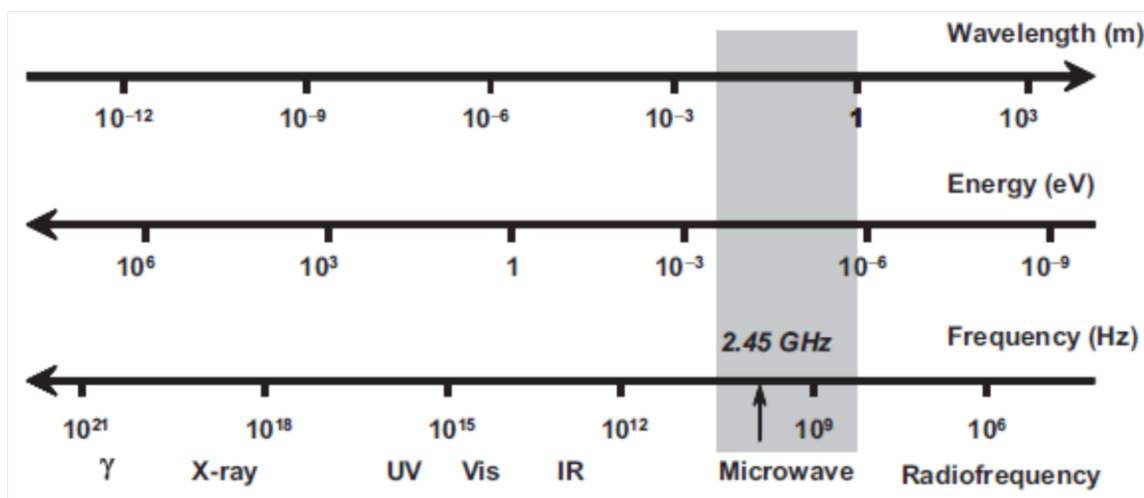
Fig 1.10 Microwave irradiation frequency range on electromagnetic spectrum. Reproduced from Practical Microwave Synthesis of Organic Chemists. *Wiley-VCH, Weinheim*, **2009**.

Microwave irradiation is a form of electromagnetic waves, which is in an electric and magnetic field component (Fig 1.9).[56] Its frequency ranges from 300 MHz to 300 GHz, which represents frequency between infrared and radio frequencies (Fig 1.10).

There are two main effects of microwave irradiation on molecules: (1) thermal effects and (2) electrostatic polar effects.

There are many reviews and articles that describe the basic overview of the microwave heating.[56,57,58,59] The thermal effects result from dipolar polarization and ionic conduction. These two mechanisms allow the electric component of the electromagnetic waves to cause heating. Dipolar polarization mechanism is when there is an interaction between the electric field component and the polar molecules. In an electric field, molecules with a permanent dipole moment are aligned to the applied field. When the electric field oscillates, the orientation of molecules also changes in response to each oscillation. During this process, the energy is lost in the form of heat due to molecular friction and dielectric loss. The amount of heat generated depends on the ability of the molecules to align themselves with the frequency of the applied field. For most microwave ovens, a frequency of 2.45 GHz is applied. Ionic conduction occurs when there is an interaction between the dissolved charged particles in a sample and their neighboring molecules. The electric component of microwave irradiation causes the dissolved charged particles in a sample to oscillate and collide with surrounded molecules, which creates heat. The second effect of microwave irradiation is the electrostatic polar effect. This effect results in dipole-dipole-type interactions between the dipolar molecules and the charges in electric field, where more polar states are more stable in the electric field.
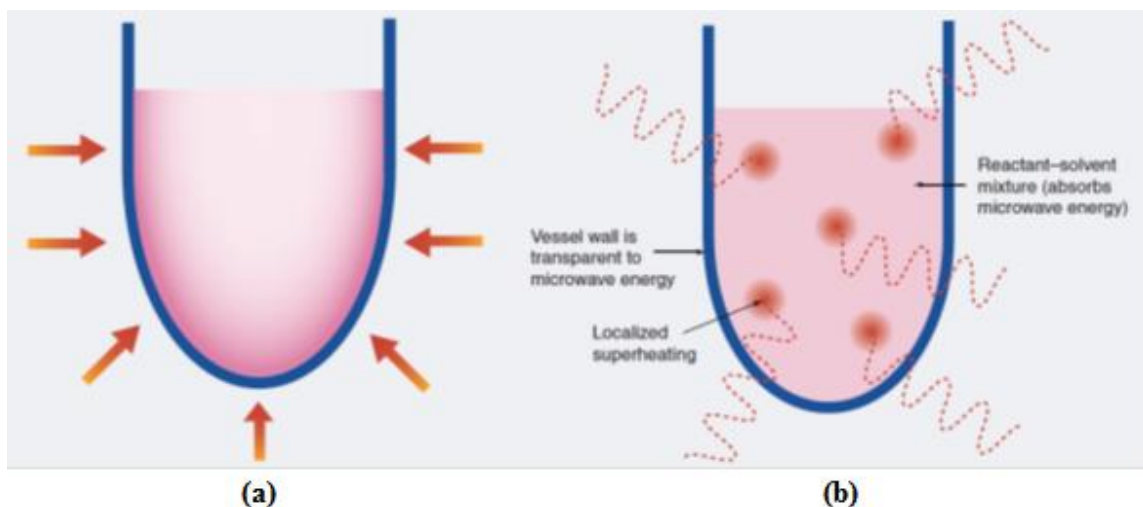
Fig 1.11 (a) Conventional heating, showing the temperature of the vessel wall is greater than the temperature of reaction solution. (b) Microwave heating, showing localized superheating. Reproduced from *Future Med. Chem.* **2010**, 2(2), 153.

As previously mentioned, microwave heating generally offers several advantages compared to conventional heating, such as shorter reaction time, better yield with less side reactions, and cleaner products. The conventional heating is time-consuming and inefficient.[60] It requires an external heating source and it requires heat to first go through the walls of the reaction vessel to be transferred to the reactants, which leads to a higher temperature of the reaction vessel than that of the reactants (Fig 1.11a). The microwave heating avoids these problems. Typically, the reaction vessels for microwave heating are made of microwave-transparent materials such as glass and Teflon, so that the radiation passes directly into the reactants and results in an inverted temperature gradient.[56,57] Also, since the microwave process is not limited by thermal conductivity of the vessel, it leads to an instantaneous localized superheating of substances (Fig 1.11b) that respond to either dipole rotation or ionic conduction. The difference between a temperature gradient and an inverted temperature gradient are represented in the schematic illustration below (Fig 1.12).
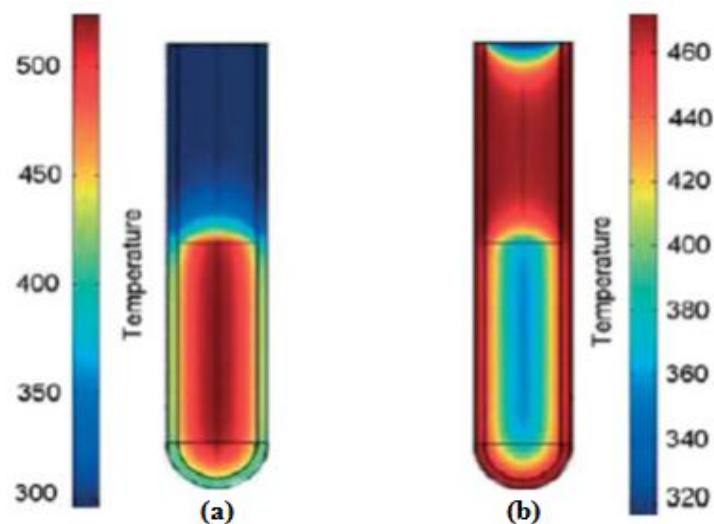
Fig 1.12 (a)Microwave heating, showing inverted temperature gradient; (b)Oil-bath heating, showing temperature gradient. Reproduced from Interaction of Microwave Irradiation with Material. Microwaves in Organic and Medicinal Chemistry. *Wiley-VCH*, *Weinheim,* **2005**.

Due to these advantages, the microwave heating has developed into a powerful tool in Chemistry, including in carbon nanoscience. Particularly, microwave heating has been a valuable tool for functionalizing carbon nanotubes.[61,62,63,64,65,66,67,68,69] Before microwave-functionalization was developed, the conventional methods were used, which were time-consuming and inefficient.[62] Fortunately, the discovery of microwave chemistry in carbon nanotube functionalization has shortened the reaction time, and increased the product yield and purity. Owing to all the benefits, in our work, microwave heating has been used on graphene sheets and carbon nanotubes in a mixture with acids to rapidly and simultaneously oxidize them, thereby producing low-oxygen containing graphene (ME-LOGr) and low-oxygen containing nanotubes (ME-MWNTs).

1.5   Sonochemistry

Over the past several decades, nanoscience and nanotechnology has been rapidly growing. For nanostructured materials, a decision on the synthetic route to prepare the

products is the key for their properties and applications.[70] As a result of extensive studies

over many years, sonochemistry is considered as one of the most useful tools to

synthesize nanostructured materials.[70]

Compared to traditional types of energy sources, sonochemistry provides high

energies and pressures within the short duration (Fig 1.13), without direct contact

between ultrasound and reactants.[70] Because of its extraordinary conditions, the use of

ultrasound has a broad range of applications in chemistry, such as synthesis,

environmental protection, and process engineering.[71]
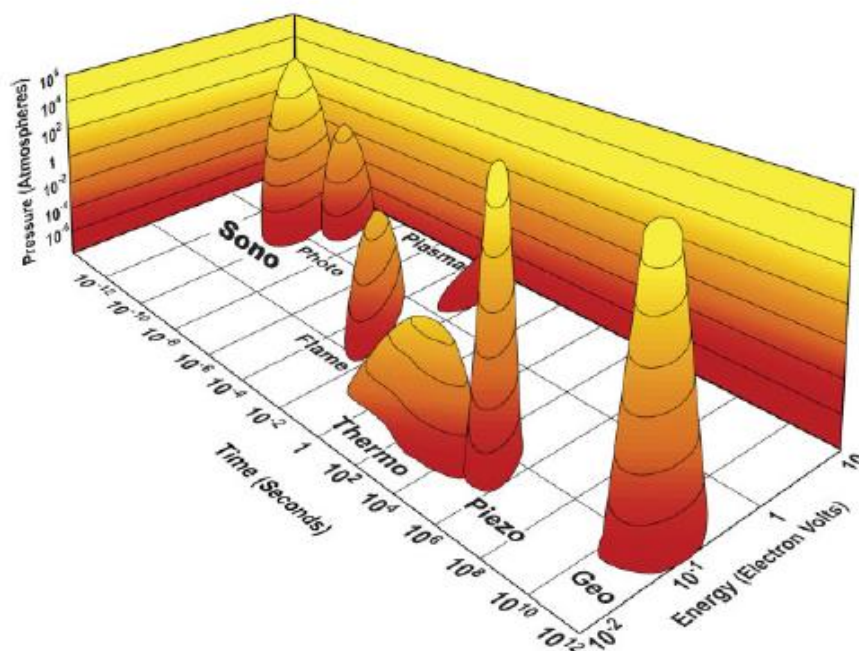
Fig 1.13 Schematic illustration showing different types of energy as a function of
time, pressure, and energy. Reproduced from *Science* **1990**, 247, 1439.
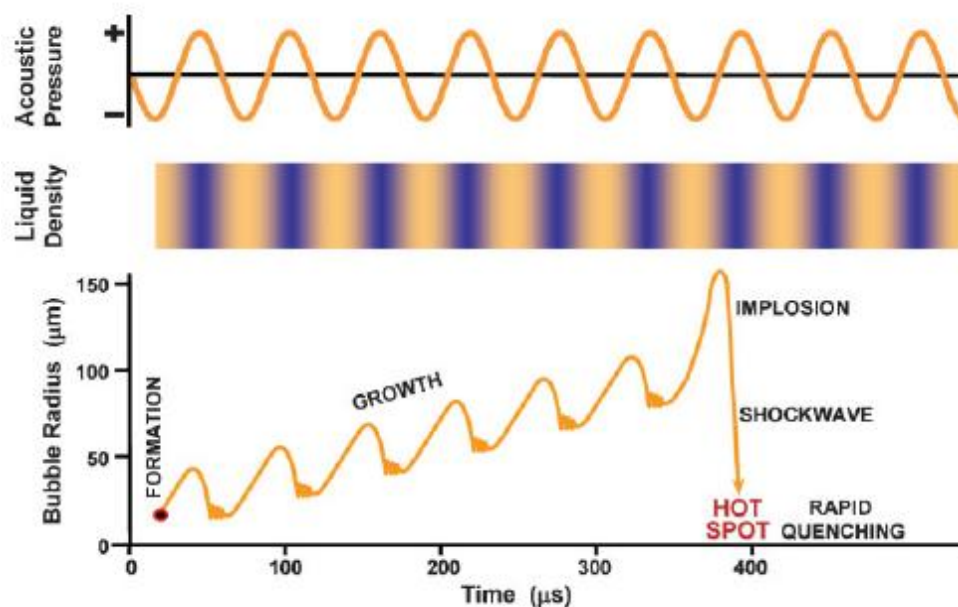
Fig 1.14 Transient acoustic cavitation. Reproduced from *MRS Bull.* **1995**, 20, 29.

Ultrasound is a sound energy with frequency of between 20 kHz and beyond 100 MHz and sonochmistry generally uses frequencies between 20 and 40 kHz for laboratory equipment purposes.[71] Similar to other sound energy, ultrasound contains a series of compression and rarefaction waves that move through a medium. As these waves alternate upon the ultrasound irradiation, cavitation bubbles are formed and they oscillate.[72] These oscillating bubbles grow in size as they accumulate ultrasonic energy, and they eventually collapse and release the energy that was accumulated in the bubble within a very short duration (Fig 1.14)[70]. This cavitational implosion releases tremendous amounts of heat and energy, giving temperatures of around 5000 K with a pressure of 1000 bar.[73]

As the source of ultrasound, all the commercial instruments use an ultrasonic transducer for generating energy, which converts mechanical or electrical energy to

sound energy. There are three main types of ultrasonic transducers: liquid-driven, magnetostrictive, and piezoelectric.[71] However, the piezoelectric transduction is the widely used for the current equipments. For the laboratory chemistry purpose, the ultrasonic cleaning bath and the ultrasonic horn are the most common sources.[71] The ultrasonic cleaning bath (Fig 1.15a) has advantages for its availability and cheap cost. For typical uses, a standard glass vessel is immersed into the bath, which requires acoustic energy to transfer through the water in the tank and the reaction vessel walls. Fortunately, a fairly even distribution of energy is provided to the medium, and an energy between 1 and 5 W cm^{-2} reaches the reaction mixture. However, control over the temperature is poor, thus it may require additional thermostatic control. Besides the ultrasonic bath, ultrasonic horn (Fig 1.15b) is also widely used.[71] It directly delivers acoustic energy into the system, which allows the reaction system to receive up to several hundred W cm^{-2}. However, it is relatively expensive and inefficient for some reactions.
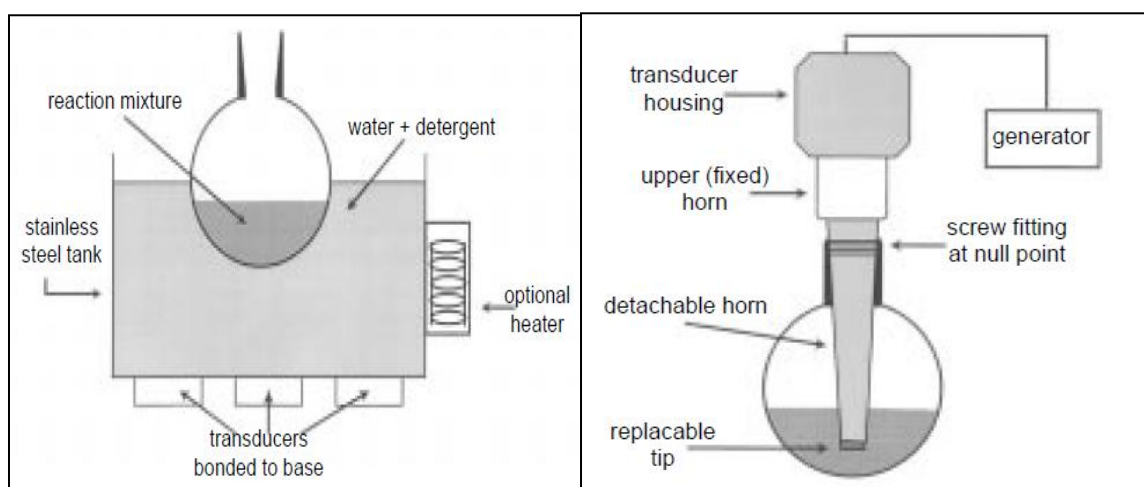
Fig 1.15 (a)Ultrasonic cleaning bath and (b)ultrasonic horn. Reproduced from *Chemical Society Reviews,* **1997**, 26, 444.

Because use of ultrasound is a powerful method in nanomaterial syntheses, much efforts was put into studying chemical effect of the ultrasound. [74,75,76,77] In water, ultrasound irradiation produces H· and OH· radicals.[77] These radicals can combine to produce its original form or H_2 and H_2O_2. In an oxygen environment, these radicals can form HO_2·. In aqueous solutions, all the products can further react as strong oxidants and reductants.

Throughout our work, we have extensively applied ultrasound irradiation using an ultrasonic cleaning bath. It has been a useful tool for many purposes, such as for dispersion and for mixing.

References

[1] Dresselhaus, M. S.; Dresselhaus, G.; Eklund, P. C. Science of Fullerenes and Carbon Nanotubes. *Academic Press,* **1996.**

[2] Kadish, K. M.; Ruoff, R. S. Fullerences: Chemistry, Physics, and Technology. Wiley-IEEE, **2000**.

[3] Hirsch, A.; Brettreich, M. Fullerences: Chemistry and Reactions. Wiley-VCH, **2005**.

[4] Kroto, H. W.; McKay, K. *Nature*, **1988**, 331, 328.

[5] Chuvilin, A.; Kaiser, U.; Bichoutskaia, E.; Besley, N. A.; Khlobystov, A. N. *Nat. Chem.* **2010**, advance online publication.

[6] Oberlin, A.; Endo, M.; Koyama, T. *J. Cryst. Growth.* **1976**, 32, 335.

[7] Iijima, S. *Nature*. **1991**, 354, 56.

[8] Novoselov, K. S.; Geim, A. K.; Morozov, S. V.; Jiang, D.; Zhang, Y.; Dubonos, S. V.; Grigorieva, I. V.; Firsov, A. A. *Science*. **2004**, 306, 666.

[9] Geim, A. K.; Novoselov, K. S. *Nature Materials*. **2007**, 6, 183-191.

[10] Novoselov, K. S.; Geim, A. K.; Morozov, S. V.; Jiang, D.; Zhang, Y.; Dubonos, S. V.; Grigorieva, I. V.; Filrsov, A. A *Science* **2004**, 306, 666–669.

[11] Novoselov, K. S.; Geim, A. K.; Morozov, S. V.; Jiang, D.; Zhang, Y.; Dubonos, S. V.; Grigorieva, I. V.; Filrsov, A. A. *Proc. Natl Acad. Sci.USA*. **2005**, 102, 10451-10453.

[12] Geim, K. Graphene: Status and Prospects. *Science.* **2009**, 324, 1530–1534.

[13] Allen, M. J.; Tung, V. C.; Kaner, R. B. *Chem. Rev.* **2010**, 110, 132–145.

[14] Rao, C. N. R.; Sood, A. K.; Subrahmanyam, K. S.; Govindaraj. *Angew. Chem., Int. Ed.* **2009**, 48, 7752–7777.

[15] Stankovich, S.; Dikin, D.; Dommett, G. H. B.; Kohlhaas, K. M.; Zimney, E. J.; Stach, E. A.; Piner, R. D.; Nguyen, S. T.; Ruoff, R. S. *Nature.* **2006**, 442, 282–286.

[16] He, H. K.; Gao, C. *Chem. Mater.* **2010**, 22, 5054–5064.

[17] Xu, Z.; Gao, C. *Macromolecules.* **2010**, 43, 6716–6723.

[18] Terrones, M.; Botello-Mendez, A. R.; Campos-Delgado, J.; Lopez-Urias, F.; Vega-Cantu, Y. I.; Rodriguez-Macias, F. J.; Elias, A. L.; Munoz-Sandoval, E.; Cano-Marquez, A. G.; Charlier, J.; Terrones, H. *Nano Today 5*. **2010**, 351-372.

[19] Elias, D. C.; Nair, R. R.; Mohiuddin, T. M. G.; Morozov, S. V.; Blake, P.; Halsall, M. P.; Ferrari, A. C.; Boukhvalov, D. W.; Katsnelson, M. I.; Geim, A. K.; Novoselv, K. S. *Science*. **2009**, 323, 610-613.

[20] Dubois, S. M.-M.; Zanolli, Z.; Declerck, X.; Charlier, J.-C. *Eur. Phys. J. B.* **2009**, 1-23.

[21] Balandin, A. A.; Ghosh, S.; Bao, W.; Calizo, I.; Teweldebrhan, D.; Miao, F.; Lau, C. N. *Nano Lett.* 2008, 8, 902.

[22] Cai, W.; Moore, A. L.; Zhu, Y.; Li, X.; Chen, S.; Shi, L.; Ruoff, R. S. *Nano Lett.* **2010**, 10, 16451.

[23] Lee, C.; Wei, X.; Kysar, J. W.; Hone, J. *Science.* **2008**, 321, 385.

[24] Frank, I. W.; Tanenbaum, D. M.; van der Zande, A. M.; McEuen, P. L. *AVS*, **2007**, 2558—2561.

[25] Lee, S.; Noh, J.H.; Bae, S.-T.; Cho, I.-S.; Kim, J. Y.; Shin, H.; Lee, J.-K.; Jung, H. S.; Hong, K. S. *J. Phys. Chem. C* **2009**, 113, 7443-7447.

[26] Dai, H. *Acc. Chem. Res.* **2002**, 35, 1035-1044.

[27] Harris, P. J. F. Carbon Nanotubes and Related Structures. *Cambridge University Press.* **1999**.

[28] Saito, R.; Dresselhaus, G.; Dresselhaus, M. S. *Imperial College Press.* **1998**.

[29] Saito, R.; Fujita, M.; Dresselhaus, G.; Dresselhaus, M. S. *Phys. Rev.B* **1992**, *46*, 1804

[30] Saito, R.; Fujita, M.; Dresselhaus, G.; Dresselhaus, M. S. *Appl. Phys. Lett.* **1992**, *60*, 2204.

[31] Mintmire, J. W.; Dunlap, B. I.; White, C. T. *Phys. Rev. Lett.* **1992**, 68, 631.

[32] Hong, S.; Myung, S. *Nature Nanotechnology*. **2007**, 2, 207-208.

[33] Barinov, A.; Gregoratti, L.; Dudin, P.; La Rosa, S.; Kiskinova, M. *Adv. Mater.* **2009**, *21*, 1916–1920.

[34] Mielke, S. L.; Troya, D.; Zhang, S.; Li, J. L.; Xiao, S. P.; Car, R.; Ruoff, R. S.; Schatz, G. C.; Belytschko, T. *Chem. Phys. Lett.* **2004**, *390*, 413–420.

[35] Sammalkorpi, M.; Krasheninnikov, A.; Kuronen, A.; Nordlund, K.; Kaski, K. *Phys. Rev. B* **2004**, *70*, 8.

[36] Yi, W.; Lu, L.; Zhang, D. L.; Pan, Z. W.; Xie, S. S. *Phys. Rev. B* **1999**, *59*, R9015–R9018.

[37] Hou, W. Y.; Xiao, S. P. *J. Nanosci. Nanotechnol.* **2007**, 7, 4478-4485.

[38] Scarpa, F.; Adhikari, S.; Wang, C. Y. *J. Phys. D* **2009**, 42, 6.

[39] Che, J. W.; Cagin, T.; Goddard, W. A. *Nanotechnology* **2000**, 11, 6569.

[40] Liu, C. H.; Fan, S. S. *Appl. Phys. Lett.* **2005**, 86, 3.

[41] Mingo, N.; Broido, D. A. *Nano Lett.* **2005**, 5, 1221-1225.

[42] Padgett, C. W.; Brenner, D. W. *Nano Lett.* **2004**, 4, 1051-1053.

[43] Monthioux, M.; Smith, B. W.; Burteaux, B.; Claye, A.; Fischer, J. E.; Luzzi, D. E. *Carbon* **2001**, 39, 1251-1272.

[44] Imholt, T. J.; Dyke, C. A.; Hasslacher, B.; Perez, J. M.; Price, D. W.; Roberts, J. A.; Scott, J. B.; Wadhawan, A.; Ye, Z.; Tour, J. M. *Chem. Mater.* **2003**, 15, 3969-3970.

[45] Wadhawan, A.; Garrett, C.; Perez, J. M. *Appl. Phys. Lett.* **2003**, 83, 2683-2685.

[46] Naab, F.; Dhoubhadel, M.; Holland, O. W.; Duggan, J. L.; Roberts, J.; McDaniel, F. D. Wiley Interscience: Portoroz, Slovenia, 2004; pp 601.1-601.4.

[47] Lin, W; Moon, K.-S.; Zhang, S.; Ding, Y.; Shang, J.; Chen, M.; Wong, C.-p. *Am. Chem. Soc.* **2010**. 4(3), 1716-1717.

[48] Vazquez, E.; Prato, M. *ACS Nano* **2009,** 3, 3819-3824.

[49] de la Cruz, P.; de la Hoz, A.; Langa, F.; Illescas, B.; Martin, N. *Tetrahedron* **1997**, 53, 2599-2608.

[50] Delgado, J.L.; Cruz, P.d.l.; Langa, F.; Urbina, A.; Casado, J.; Navarrete, J.T.L. *Chem. Commun.* **2004**, 1734-1735.

[51] Umeyama, T.; Tezuka, N.; Fujita, M.; Matano, Y.; Takeda, N.; Murakoshi, K.; Yoshida, K.; Isoda, S.; Imahori, H. *J. Phys. Chem. C* **2007**, 111, 9734-9741.

[52] Brunetti, F.G.; Herrero, M.A.; Munnoz, J.d.M.; Giordani, S.; Diaz-Ortiz, A.; Filippone, S.; Ruaro, G.; Meneghetti, M.; Prato, M.; Vazquez, E. *J. Am. Chem. Soc.* **2007,** 129, 14580-14581.

[53] Brunetti, F.G.; Herrero, M.A.; Munnoz, J.d.M.; Diaz-Ortiz, A.; Alfonsi, J.; Meneghetti, M.; Prato, M.; Vazquez, E. *J. Am. Chem. Soc.* **2008**, 130, 8097-8100.

[54] Rubio, N.; Herrero, M.A.; Meneghetti, M.; Diaz-Ortiz, A.; Schiavon, M.; Prato, M.; Vazquez, E. *J. Mater Chem.* **2009**, 19, 4407-4413.

[55] Kempe, K.; Becer, C.R.; Schubert, U.S. *Am. Chem. Soc.* **2011.** 44, 5825-5842.

[56] Kappe, C.O.; Dallinger, C.; Murphree, S.S. Practical Microwave Synthesis of Organic Chemists. Wiley-VCH, Weinheim, 2009.

[57] Kappe, C.O.; Stadler, A. Microwaves in Organic and Medicinal Chemistry, Wiley-VCH, Weinheim, 2005.

[58] Loupy, A. (Ed.). Microwaves in Organic Synthesis, Wiley-VCH, Weinheim, 2006.

[59] Lew, A.; Krutzik, P.O.; Hart, M.E.; Chamberlin, A.R. *Am. Chem. Soc.* **2002**. 4, 2, 95-105.

[60] Collins, M. J. *Future Med. Chem.* **2010**, 2(2), 151-155.

[61] Delgado, J. L.; De la Cruz, P.; Langa, F.; Urbina, A.; Casado, J.; Lopez Navarrete, J. T. *Chem. Commun.* **2004**, 1734-1735.

[62] Wang, Y.; Iqbal, Z.; Itra, S. *J. Am. Chem. Soc.* **2006**, 128, 95-99.

[63] Raghuveer, M. S.; Angrawal, S.; Bishop, N.; Ramanath, G. *Chem. Mater.* **2006**, 18, 1390-1393.

[64] Brunetti, F. G.; Herrero, M. A.; de, M.; Munoz, J.; Giordani, S.; Diaz-Ortiz, A.; Filippone, S.; Ruaro, G.; Meneghetti, M.; Prato, P.; Va'zquez, E. *J. Am. Chem. Soc.* **2007**, 129, 14580-14581.

[65] Liu, J.; Zubiri, M. R. I.; Vigolo, B.; Dossot, M.; Fort, Y.; Ehrhardt, J. J.; McRae, E. *Carbon* **2007**, 45, 885-891.

[66] Kakade, B. A.; Pillai, V. K. *Appl. Surf. Sci.* **2008**, 254, 4936-4943.

[67] Colomer, J. F.; Marenga, R.; Traboulsi, H.; Meneghetti, M.; Tendeloo, G. V.; Bonifazi, D. *Chem. Mater.* **2009**, 21, 4747-4749.

[68] Lin, W.; Zhang, R. W.; Moon, K. S.; Wong, C. P. *Carbon* **2010**, 48, 107-113.

[69] Economopoulos, S. P.; Pagona, G.; Yudasaka, M.; Iijima, S.; Tagmatarchis, N. *J. Mater. Chem.* **2009**, 19, 7326-7331.

[70] Bang, J. H.; Suslick, K. S. *Adv. Mater.* **2010**, 22, 1039-1059.

[71] Mason, T. J. *Chemical Society Reviews,* **1997**, 26, 443-451.

[72] Suslick, K. S.; Doktycz, S. J. Advances in Sonochemistry. Ed.: Mason, T. J., *JAI Press*, New York. **1990**, pp 197.

[73] Suslick, K. S. *Science* **1990**, 247, 1439.

[74] Weissler, A. *J. Am. Chem. Soc.* **1959**, 81, 1077

[75] Weissler, A. *Nature.* **1962**, 193, 1070.

[76] Anbar, M.; Pecht, I. *J. Phys. Chem.* **1964**, 68, 352.

[77] Makino, K.; Mossoba, M. M.; Riesz, P. *J. Am. Chem. Soc.* **1982**, 104, 3537.

CHAPTER 2   Improvement on Conductivity of Multi-walled Carbon

Nanotube/Graphene Hybrid Film by Crosslinking

2.1   Introduction

Since the first discovery by Iijima in 1991[1], carbon nanotubes (CNTs) received great attention due to their extraordinary properties such as outstanding chemical stability, electron transfer, mechanical strength, high aspect ratio, and flexibility.[2] Because of their unique properties, CNTs have been considered as most promising nanomaterial for fabricating flexible electric devices, such as field effect transistors.[3456] There is increasing enthusiasm for the use of carbon nanotube network films as conductive flexible electrodes and sensing materials due to the following advantages.[7] CNT films can be readily fabricated by several room temperature solution based processes, such as spray coating,[1-2] and deposition through a filter.[3-4] The obtained networks are highly reproducible due to statistical averaging effects and exhibit percolation-like electrical conductivity. SWNT networks have been demonstrated to function for a variety of applications including electrodes for solar cells,[5] organic light emitting diode,[6] smart windows,[7] sensors,[8] and transparent transistors.[2] There have been several reports on the conductivity of CNT networks, with values ranging from 12.5 S/cm[9] to ~ 6600 S/cm.[3,10], which are significantly lower than the conductivity of a CNT rope[11-12] due to the existence of high resistance and tunneling/Schottky barriers at the intertube junctions, which dominates the overall film resistance in the network film.

Graphene, a single layer of carbon, as a rising star in material science, exhibits remarkable properties for various novel applications. Graphene is essentially a single walled carbon nanotube (SWNT) cut along its axis and unrolled to lay flat. Conductive films from graphene sheets share the same advantages as CNTs for conductive and transparent electrodes as mentioned above. However, it is much cheaper. More importantly, it can provide conduction pathways to a greater area per unit mass than SWNTs, which should translate into dramatically improved conductivity and high transparency.[15] Nevertheless, the electronic performance of thin films from neither CNTs nor graphene has reached their theoretical expectations.

Recently, several reports have proposed to fabricate a hybrid film by combining the merit of the carbon nanotubes and graphene to have further improved conductivity.[8,9] Yang and co-workers successfully synthesized hydrazine-reduced hybrid films of single-walled nanotubes (SWNT) and graphene oxide (GO), which showed improved sheet resistance and transmittance compared to either SWNT-only or graphene-only films.[10] They used dry powders of GO that was synthesized from a modified Hummers method and slightly oxidized SWNTs to combine them together in anhydrous hydrazine by sonication. The resulted film displayed a sheet resistance of 240 Ω/sq at 86% transmittance. However, for industrial applications, the cost for the hydrazine reduction process is relatively expensive and the toxicity of hydrazine is another problem. Another attempt at preparing transparent conducting SWNT/graphene hybrid film has been made by Colman and co-workers.[8] Unlike Yang et al., they prepared solution-processable graphene and SWNTs by adding sodium cholate (NaC) as the surfactant. Then, they sonicated them together, followed by vacuum filtration to fabricate the hybrid film. They

have optimized the weight fraction of graphene for electrical and optical properties and

found that 3 wt% graphene provides the film with the highest sheet conductance, 1.2×10^5

S/m, without reducing the optical transmittance.[8] Although this process avoided the use

of hazardous hydrazine by using surfactant to disperse the graphite, the residual

surfactants can dramatically decrease the overall electrical conductivity by increasing the

resistance between the individual graphene sheets. While Yang et al. and Colmen et al.

used SWNTs for fabrication of hybrid films, Kim and co-workers used multi-walled

nanotubes (MWNTs) to combine with reduced graphene oxide (RGO) for synthesizing

transparent, flexible conducting hybrid multilayer thin films using layer-by-layer (LBL)

assembly.[11] Electrostatic interactions between negatively charged RGO and positively

charged MWNTs were the driving force in their film fabrication process, which produced

a hybrid film with sheet resistance of 8 kΩ/sq at 81 % transmittance and average film

thickness of 11 nm, after thermal treatment.[11] This method allowed excellent control over

the optical and electrical properties of the hybrid film. However, this method was rather

time-consuming and costly, since it requires many chemicals to synthesize charged RGO

and MWNTs.

In the present study, we present the fabrication of conducting MWNTs/graphene

hybrid films using microwave-enabled low-oxygen MWNTs (ME-LOMWNTs) and

microwave-enabled low-oxygen graphene (ME-LOGr), which was introduced in our

previous work.[10] By using microwave heating in a mixture of concentrated acids (HNO_3

and H_2SO_4 in 1:1 volume ratio), large and highly conductive solution-processable ME-

LOGr, are directly formed without need of a reduction process. The combination of

microwave heating and aromatic oxidation by nitronium ions allows producing a

minimum concentration of oxygen moieties required for separation of graphene sheets by simultaneous oxidation of carbon atoms. Fig 2.1a shows result of X-ray photoelectron spectroscopy (XPS) for ME-LOGr. The spectrum shows the percentages of graphitic carbon, non-oxidized carbon, on the ME-LOGr sample. A 79% of the spectrum shows the oxygen-free carbon of ME-LOGr, which indicates that the ME-LOGr contains only small amount of oxygen-containing groups.[10] This process does not involve either hydrazine or surfactant, since it does not require a reduction process to restore the conductivity of the graphene. Using very similar procedures and parameters, we directly dispersed MWNTs into water solutions (Fig 2.2). Following the terminology of microwave-enabled low-oxygen graphene (ME-LOGr), we refer to the dispersed MWNTs as microwave-enabled low-oxygen MWNTs (ME-LOMWNTs). With a help from colleague, XPS spectrum of ME-LOMWNT was obtained, in which the oxygen-free carbon of ME-LOMWNT makes up 74% of the spectrum (Fig 2.1b). A detailed study on determining the oxygen containing groups of ME-LOMWNT is still in progress.
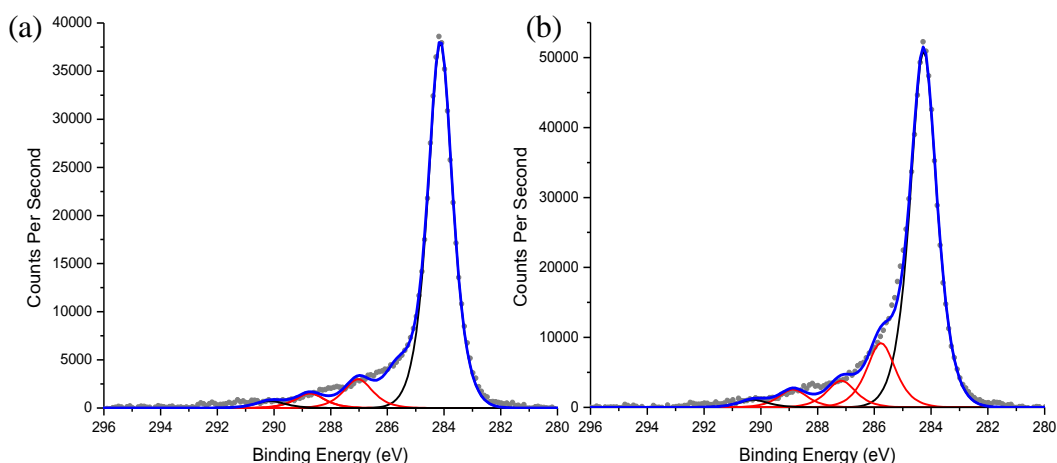
Fig 2.1 XPS spectra of (a) ME-LOGr and (b) ME-LOMWNT

(a)　　**(b)**　　**(c)**　　**(d)**
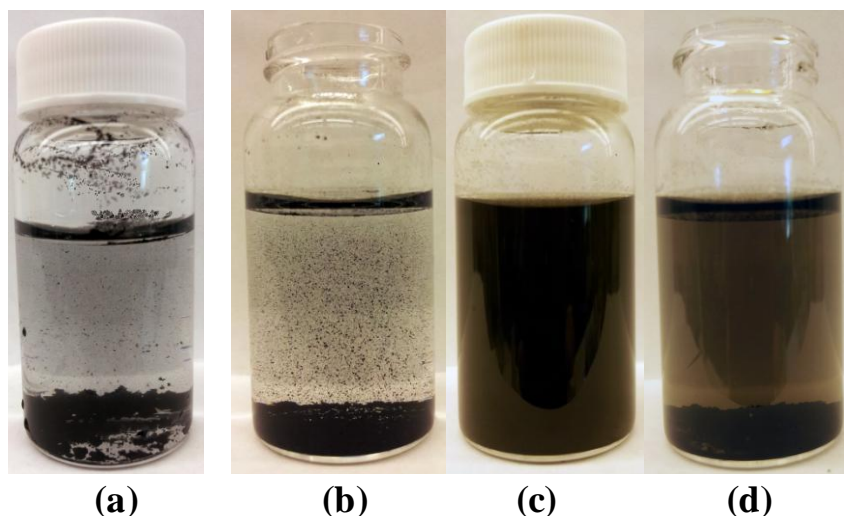
Fig 2.2 Digital photographs of: (a)MWNTs sonicated in water for 1 hour; (b)ME-LOMWNTs, before the dispersion; (c)ME-LOMWNTs, after the dispersion in bath sonication for 1 hour; (d)dispersed ME-LOMWNTs, after 5 days at room temperature.

Using the ME-LOMWNT and ME-LOGr, this work aims to improve the conductivity and mechanical integrity of hybrid carbon nanotube and graphene films. Within the work, we discovered that the microwave-enabled low oxygen containing carbon nanomaterials are crosslinked, which enhances the conductivity and mechanical strength of the hybrid films. Therefore, the main key to further improve the electrical and mechanical properties of the films is to encourage the crosslinking between ME-LOMWNTs and ME-LOGr. As a way to increase the degree of crosslinking, we introduced concentrated acidic environment during the film fabrication. This new approached was inspired by a reported work of graphene oxide decomposition into tiny fragments of soluble polycyclic aromatic hydrocarbons (PAHs) and synthesis of fullerenes and nanotubes from these PAHs by sonication in dehydrated acidic environment.[11] The mechanism behind the PAHs forming fullerenes and nanotubes by sonication in the acidic medium was that biaryl coupling and nucleation were favored by intramolecular or intermolecular dehydration reactions between the edges of these PAHs.

We expected these dehydration reactions to occur between the edges of MWNTs and graphene sheets as we introduce the acidic environment, so that the degree of crosslinking increases and therefore enhances the conductivity and mechanical strength of the ME-LOMWNT/ME-LOGr hybrid films. Our results support this hypothesis and the hybrid films show a conductivity of 24,979 S m^{-1}, which is two times higher than those reported by Colman and co-workers.[8] The capability to extremely rapidly (30s) and cost effectively fabricate large amounts of high quality dispersed MWNTs and graphene sheets, and the capability to form highly conductive hybrid films from these carbon nanomaterials should enable a broad range of real-world applications.

2.2   Experimental procedure

2.2.1   Chemicals

Graphite powder (~20 μm) was purchased from Sigma Aldrich and used as received. Multi-walled Nanotube powder was received from China and also used as received. ACS grade concentrated sulfuric acid (98% H_2SO_4) and concentrated nitric acid (70% HNO_3) were purchased from Pharmco-AAPER and used as received. Deionized water (18.2 MΩ) (Nanopore water, Barnstead) was used to prepare all solutions, as well as to rinse and clean the samples.

2.2.2   Direct synthesis of microwave-enabled low-oxygen graphene (ME-LOGr)

In a round-bottomed flask, 20 mg of the as-purchased graphite (Sigma-Aldrich, ~20 μm) were suspended in 1:1 98% H_2SO_4/70 %HNO_3 (total volume of 10 mL), and swirled to mix. Then, the mixture was placed into a microwave reactor (CEM-Discover) chamber.

The placed flask was connected to a reflux condenser and reacted with the power set at 300 W for 30 sec. In order to directly obtain a colloidal ME-LOGr solution, the formed suspension was filtered through a polycarbonate track-etch filter membrane (0.2 μm pore size; Watman Ltd.), and was washed three times with deionized water (200 mL each time) to remove the excess acid. Then, the filtrand was re-dispersed into water by sonicating for 30 minutes in a sonication bath. The obtained grey ME-LOGr dispersion was set at room temperature for at least 48 hours before it was used.

2.2.3 Direct synthesis of microwave-enabled low-oxygen MWNT (ME-LOMWNTs)

The same procedure for synthesizing ME-LOGr was performed with 5mg of MWNTs (received from China).

2.2.4 Synthesis and optimization of ME-LOMWNTs/ME-LOGr hybrid films

For each composite solution in this experiment, the total weight of carbon nanomaterials (ME-LOMWNTs or ME-LOGr) in the solution was maintained at 0.5 mg.

The total weight of carbon nanomaterials was obtained by obtaining calibration curve of optical absorption as a function of weight of the ME-LOMWNTs and ME-LOGr, respectively. During the synthesis of ME-LOGr, the dry filtrand after acid clean-up was collected and the weight was measured. A known amount of water was added to calculate the concentration (concentration = mass of solute/total volume of solvent). After 30 minutes of bath sonicating, the absorption spectrum of dispersed ME-LOGr solution with known concentration was taken and recorded on a Cary 500 UV-vis-NIR spectrophotometer in double-beam mode using 1 cm quartz cuvettes. The range of

wavelength taken was between 800 nm and 200 nm. The UV-vis spectrum of the ME-LOGr solution displayed an absorption maximum at 267 nm. By diluting the solution with known amount of water, UV-vis spectra were recorded for five different concentrations of the solution. When all the spectra were recorded, the absorbance at the absorption maximum (267 nm) for each spectrum was obtained. Then, a graph of absorbance versus concentration was plotted. On the plot, data was fitted with a straight line to determine the slope and its uncertainty. With the determined slope and uncertainty, an equation was formulated in the following format: $y = mx + b$, where m is the slope and b is the uncertainty. For ME-LOGr, the resulting equation was, $y = 8.3348x + 0.019$. With this equation, as we synthesize the ME-LOGr solution with unknown concentration, we recorded UV-vis spectrum to determine the absorbance at the absorption maximum wavelength. As the absorbance was determined, it was plugged into the equation as a y value, and the concentration, x, was calculated. Then, with the calculated concentration, the required volume of solution to get certain weight of carbon nanomaterials was calculated with the concentration equation.

The volume of ME-LOMWNT solution needed was determined in the same manner, where the absorption maximum or ME-LOMWNT is at 262 nm. The resulting equation for ME-LOMWNT was: $y = 87.835x + 0.1142$.

Using this procedure, the appropriate volume of synthesized ME-LOMWNT solution and ME-LOGr solution were added in each vial with following ratios by carbon nanomaterials weight: (ME-LOMWNT/ME-LOGr) 100/0, 90/10, 50/50, 25/75. Each solution with different ratio was mixed in a sonication bath for an hour. The composite solutions were set at room temperature for 24 hours. Then, each film was obtained by

filtering through an Isopore, polycarbonate track-etch filter membrane (0.22 μm pore size; Millipore). The fabricated films on the filter membrane were dried in oven for 2 hours (at ~80 °C).

The ratio of MF-MWNT and ME-LOGr in the mixture solution was further optimized with ratio of 95/5 and 97/3 by carbon weight. The procedure of synthesizing mixture solutions in these ratios was conducted in the same way.

2.2.5   Synthesis of hybrid film in acidic environment

The same procedure was performed to prepare the mixture solution of ME-LOGr and ME-LOMWNTs, except that the re-dispersion after removing the excess acid by filtration was excluded. After removing the acid by washing the filtrand of ME-LOGr or ME-LOMWNT on the filtration membrane, the dry filtrand of ME-LOGr and ME-LOMWNT were collected. Instead of re-dispersing them in water, the collected dried products of ME-LOGr and ME-LOMWNT were added in a vial at 97/3 weight ratio. The mixture of dried products was dispersed in concentrated H_2SO_4 using bath sonication for 1 hour. Then, the obtained dispersion was set at room temperature for 24 hours. Almost all the carbon nanomaterials precipitated on the bottom of the flask as "fluffy" precipitation. The film was obtained by shaking the solution to get the "fluffy" precipitation into the solution and filtering through an Isopore, polycarbonate track-etch filter membrane (0.22 μm pore size; Millipore).

A control experiment was performed by dispersing the mixture of dried products in water with the same time (an hour) of bath sonication. Unlike the synthesized solution in acidic

environment, only a small amount of precipitation was observed. In addition, the precipitated material was not "fluffy".

2.2.6   Characterizations and measurements

2.2.6a Electrical property of hybrid films

For the composite solutions with different weight ratios of ME-LOMWNT and ME-LOGr, UV-vis-NIR absorption spectra with wavelength ranging 200nm to 800nm were obtained using a Cary 500 Ultraviolet-visible-near-infrared spectrophotometer in double-beam mode. For sheet resistance measurement of the films, a manual four point resistivity probe (Lucas Laboratories, model 302) was applied to measure the sheet resistance of the hybrid films prepared by vacuum filtration through an Isopore, polycarbonate track-etch filter membrane (0.22 µm pore size; Millipore).

2.2.6b Scanning electron microscope (SEM)

For characterizing the composite solutions, SEM samples were prepared by depositing the solution onto a SiO_2/Si substrate. The substrate was first cleaned with a UV/Ozone treatment for 10 minutes, and then in piranha solution for 15 minutes, followed by 15 minutes in water using bath sonication. Then, the substrates were modified with 2% Aminopropyltriethoxysilane (APTES) solution in toluene. The modified substrates were fully covered with each of the composite solutions by adding a drop of solution on the substrate. Then, the substrate was dried in room temperature. High contrast SEM images of the hybrid films with different ratio of ME-LOMWNT and ME-LOGr were obtained using a Hitachi S-4800 field emission scanning electron microscope (FE-SEM, Hitachi

Co. Ltd. S-4800) under small accelerating voltage (1-2 KV) and a high probe current (15-20 μA).

2.2.6c Raman spectroscopy

Raman spectroscopy was used to get information about defect of carbon on the hybrid film that was fabricated by sonicating in acid environment and its control film that was sonicated in water. Samples for Raman spectroscopy were prepared by filtering each composite solution through an Anodisc with support ring, aluminum oxide anopore membrane (0.2 μm pore size; Whatman Ltd.) and drying it in an oven (~80°C) for 2 hours. Raman spectra of the deposited films on the alumina membrane were collected in a Kaiser Optical Systems Raman Microprobe with a 785 nm solid state diode laser. Spectra were acquired using a 30 second exposure time.

2.2.6d Atomic force microscopy (AFM)

The thickness of the hybrid films was measured using a Nanoscope IIIa multimode SPM (Digital Instrument) with a J scanner operated in "Tapping Mode". AFM samples were prepared by cutting the little piece of the films on Isopore, polycarbonate track-etch filter membrane (0.22 μm pore size; Millipore). A 160 μm long rectangular silicon cantilever/tip assembly (Model: MPP-12100, Veeco) with a resonance frequency of 160 kHz, a spring constant of 7.7 N/m, and tip radius of less than 10nm was used for imaging. The scanning was performed at a rate of ~0.7 Hz. The thickness of the films was obtained by measuring average height difference between film and bare filter membrane from section analysis of the topographic images.

2.3   Results and discussion

2.3.1. UV-Vis spectroscopy of ME-LOMWNTs and ME-LOGr

Fig 2.2 displays the UV-vis-near-IR spectra of the composite solution along with

the spectra of ME-LOMWNT and ME-LOGr solution (Fig 2.3).
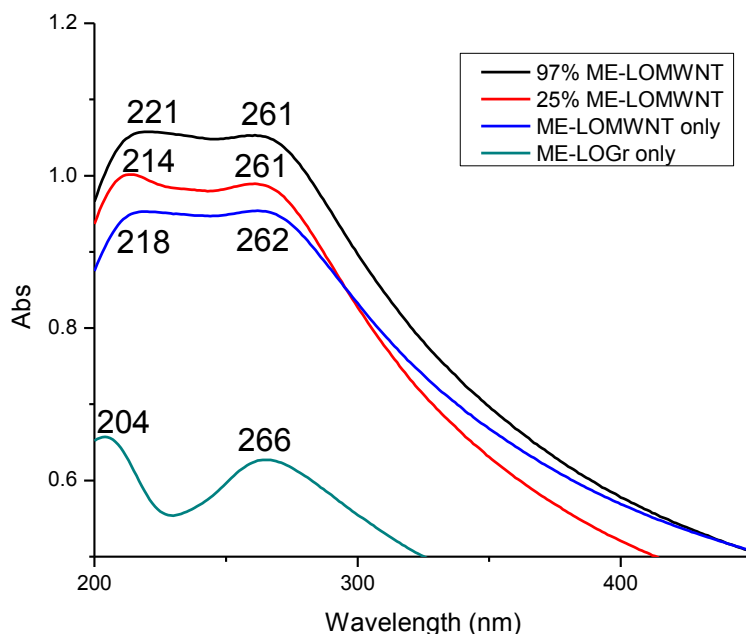
Fig 2.3 UV-vis spectra of ME-LOGr(**green**), ME-LOMWNT(**blue**), and composite
solutions with a weight ratio of ME-LOMWNTs/ME-LOGr =97/3(**black**) and =
25/75(**red**)

The UV-vis-near-IR spectra displayed interesting, rather important features for

optical property of ME-LOGr and microwave-dispersed MWNT (ME-LOMWNT). The

color of ME-LOGr suspensions is grayish-black, which qualitatively suggests that we

have directly obtained electrically conductive graphene sheets instead of the typically

brown GO solutions.[12-13] Additionally, unlike GO, the UV-Vis-Near IR spectrum of the

ME-LOGr solution displayed relatively uniform absorption in the visible and NIR region,

which suggests that the π-conjugation within the graphene sheets is largely

retained.[15,14,15] In the ultraviolet region, there are two peaks which have absorption

maximum at 205 nm and 266 nm, respectively. It was known that graphite exhibits two π plasmon bands (collective oscillations of π electrons) in the ultraviolet frequency region, which originate from the anisotropic optical properties of graphite.[16,17] The imaginary parts of the dielectric function in the direction perpendicular to the c-axis of graphite ($I_m\{\varepsilon_\perp\}$) has a maximum at 4.5 eV (275.8 nm) and the other in the direction parallel to the c-axis ($I_m\{-\varepsilon_{/\!/}^{-1}\}$ is at ~ 5.25 eV (236 nm).[9] These two peaks are commonly observed in many materials, such as carbon nanotubes, C_{60}, and amorphous carbon.[18,19,20,21,22,23,24,25] While the peak positions may vary depending on the geometries of the carbon materials and the existence of defects in the carbon materials. The absorption maximum at 204 nm and 266 nm in the ME-LOGr may originate from the $I_m\{-\varepsilon_{/\!/}^{-1}\}$ and $I_m\{\varepsilon_\perp\}$, respectively. The position of the $I_m\{\varepsilon_\perp\}$ peak has been widely used to qualitatively evaluate the oxidation level of graphene sheets. For example, the graphene sheets peeled by a Scotch tape, exhibit a peak at 275.8 nm, similar to the position in graphite. In contract, the peak in graphene oxide (GO) obtained from Hummer or modified Hummers method is around 237 nm. The peak would red-shift with chemical or thermal reduction. The ME-LOGr solution displayed an absorption maximum at 266 nm without requirement for any chemical and thermal reduction, indicating the existence of some defects such as oxygen containing groups in the graphene sheets, but the π-conjugation within the graphene sheets is largely retained. We did not find any literature reports about the peak of $I_m\{-\varepsilon_{/\!/}^{-1}\}$ in graphene. It is not clear yet at this stage how the peak position of $I_m\{-\varepsilon_{/\!/}^{-1}\}$ would change with its oxidation level. We hypothesize that the large blue shift also relates to the oxidation level of the graphene sheets.

Using the same parameters to disperse MWNTs, MWNT suspension was also

obtained. The UV-Vis spectrum of the MWNT solution is displayed in Fig 2.3 (blue

curve). The MWNT shows a fairly strong absorbance in the visible region, which is

typical of MWNT dispersed in aqueous and organic solutions. Similar to the ME-LOGr

solution, the MWNT solution also shows two peaks in the ultraviolet region, which also

originate from the maxima in $I_m\{\varepsilon_\perp\}$ and $I_m\{-\varepsilon_\parallel^{-1}\}$ and correspond to orientations parallel

and perpendicular to the MWNT axis, respectively. However, compared to those

exhibited in ME-LOGr, the maximum absorption for $I_m\{-\varepsilon_\parallel^{-1}\}$ was slightly red shifted to

218 nm, and the maximum absorption for $I_m\{\varepsilon_\perp\}$ was slightly blue shifted to 262 nm.

2.3.2. Fabrication of ME-LOMWNT/ME-LOGr hybrid films and electronic characterization of the fabricated films.

| (a) | (b) | (c) | (d) | (e) |
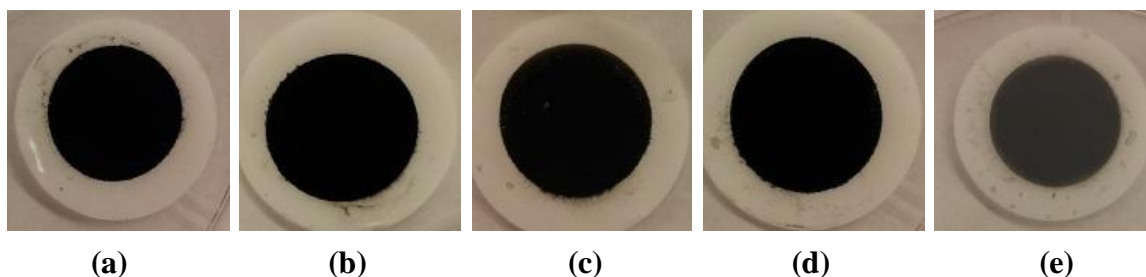
Fig 2.4 Digital photographs of ME-LOMWNTs/ME-LOGr hybrid films in weight ratio of (ME-LOMWNT/ME-LOGr): (a)100/0, (b)90/10, (c)50/50, (d)25/75, and (e)0/100

As briefly mentioned above, the ME-LOMWNT/ME-LOGr hybrid films were

obtained by typical vacuum filtration and drying in an oven for 2 hours at around 80 °C.

In a typical experiment, colloidal solutions of ME-LOMWNT and ME-LOGr are

combined using bath sonication in water. The sonication process produced the dispersed

suspensions that were used to fabricate dark, thick ME-LOMWNT/ME-LOGr hybrid films via simple vacuum filtration (Fig 2.4).

The sheet resistances of the corresponding hybrid films were measured. In order to calculate the sheet conductance, the thickness of the film was measured using AFM. Based on the collected AFM images, the surfaces of the films were very rough as the height of films was uneven. Therefore, the average height difference between the film and the bare filter membrane was used for the film thickness (Fig 2.5).

Fig 2.5 Image of film-thickness measurement. using Nanoscope 8.15. a)AFM image of hybrid film (wt% ME-LOMWNTs/ME-LOGr = 90/10) deposited on a polycarbonate filter membrane; (b)graph that represents the surface height
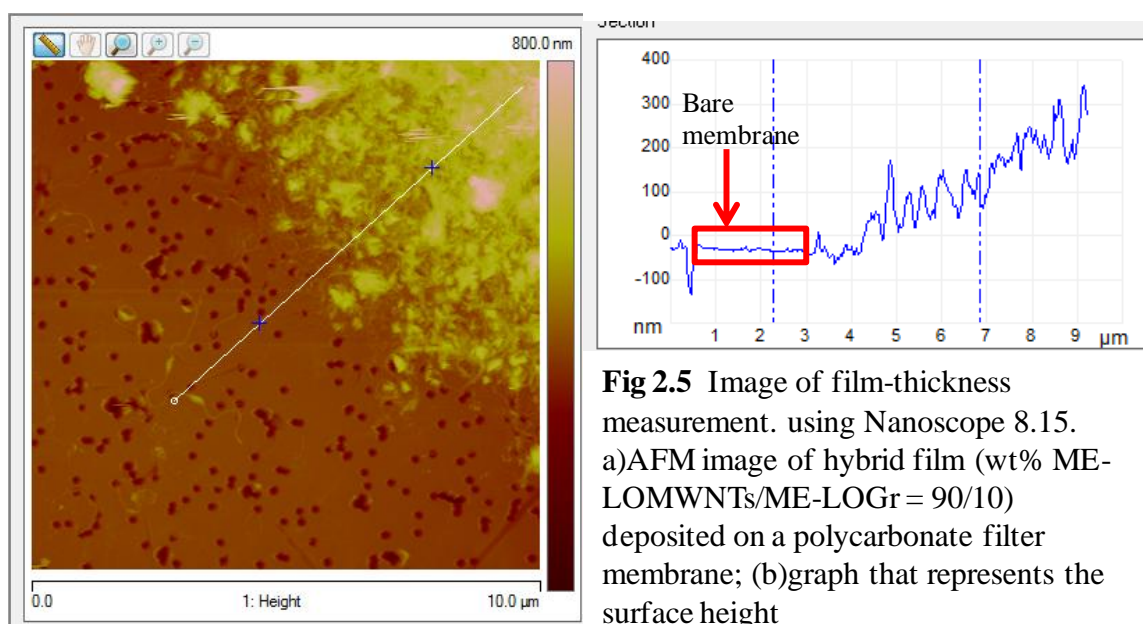
Once the sheet resistance and film thickness were measured, the sheet conductance of the corresponding film was determined by using the following equation: Sheet conductance(S/m) = 1/[Sheet resistance(Ω/sq) $\times$ film thickness(m)]. The results in Fig 2.6a revealed that ME-LOMWNT/ME-LOGr hybrid film displayed improved sheet conductance relative to either ME-LOMWNT-only or ME-LOGr-only films. Compared to the ME-LOMWNT-only film, the most conductive film with a composition of ME-LOMWNT/ME-LOGr = 97/3, showed 35% of improvement on the sheet conductance.

While, compared to the ME-LOGr-only film, the conductance of the hybrid film increased more than 30 times. Interestingly, the result was similar to the work reported by Coleman et al,[8] where 3 wt% of graphene had resulted in the most conductive hybrid film, but our sheet conductance is two times higher than that of their SWNT/graphene hybrid films.

(a)

ME-LOMWNT/ ME-LOGr	Avg sheet Resistance (Ω/sq)	Avg sheet Conductance (S/m)	Film Thickness (nm)
100/0	35.4	183937	154
97/3	28.2	247812	143
95/5	28.8	234965	148
90/10	28.7	220604	158
50/50	69.0	58507	248
25/75	125	34168	235
0/100	754	8336	161

(b)
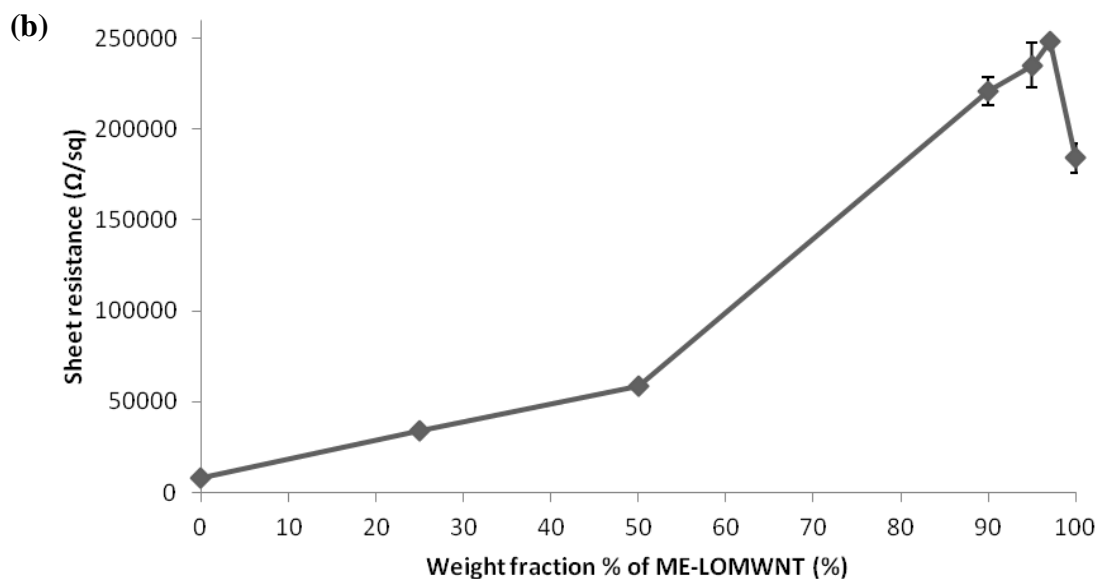
Fig 2.6 (a)Sheet resistance and conductance of ME-LOMWNTs/ME-LOGr hybrid films. (b)Sheet conductance of the hybrid films as a function of the weight percentage of ME-LOMWNTs

2.3.3 Characterization of the hybrid films by Scanning Electron Microscope (SEM)

With these results in mind, we were curious about how the carbon nanotubes and graphene are arranged in the films. Using SEM, we imaged the hybrid films which were prepared on the alumina membranes (Fig 2.7). The SEM images displayed percolation structures within the films, where ME-LOMWNTs and ME-LOGr are highly entangled with each other. Also, the ratio of ME-LOMWNTs to ME-LOGr contents on the images roughly represented the actual weight ratio of the films.
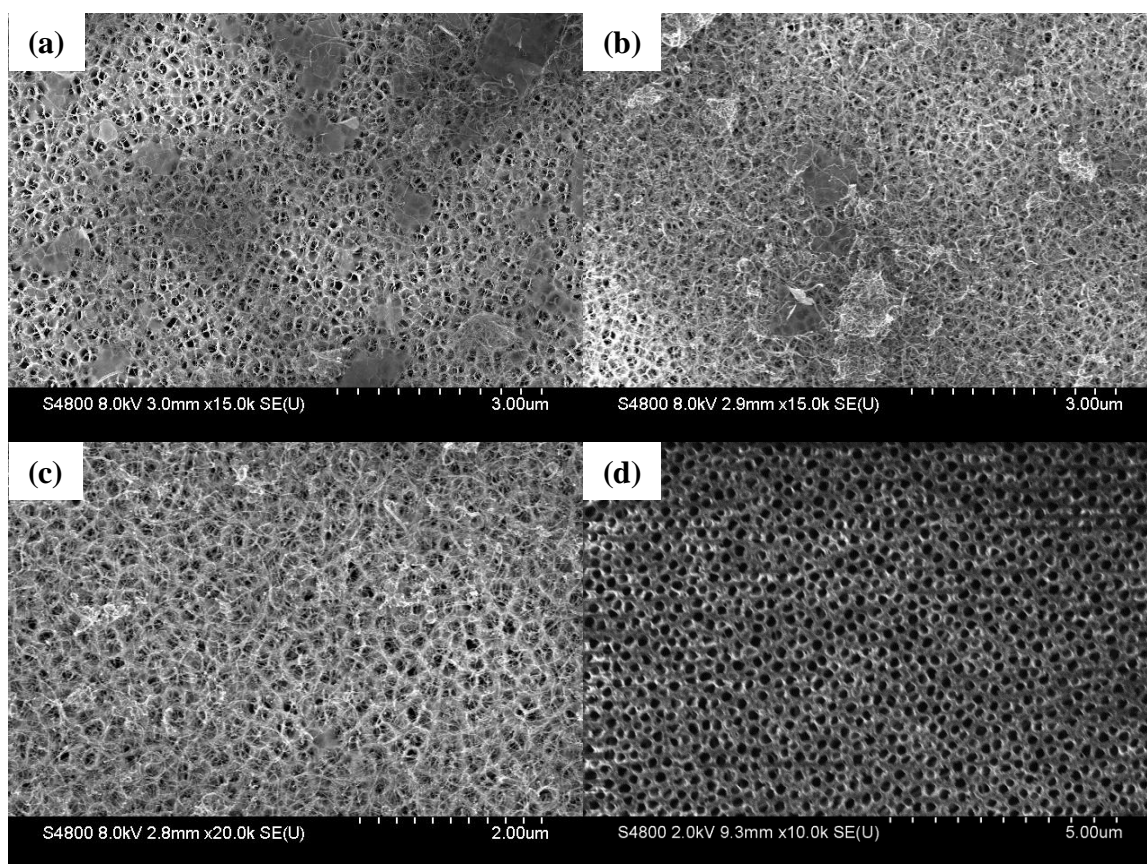
Fig 2.7 SEM images of hybrid films deposited on alumina membrane with a weight ratio of (ME-LOMWNTs/ME-LOGr): (a)25/75, (b)50/50, (c)90/10, and (d) SEM image of bare alumina membrane.

Most importantly, we have found that the some of ME-LOMWNTs and ME-LOGr crosslinked with each other. (Fig 2.8, indicated by red circles). The crosslinks appeared in

a way that the carbon nanotubes are "growing" out from the graphene sheet (indicated by red circles on Fig 2.7a~c). By carefully observing the SEM images, it is possible that crosslinking also happens between ME-LOMWNTs (Fig 2.7d). This observation is very important in that the observed enhancement of conductivity in the hybrid films is possibly due to these crosslinks, by which some of the MWNTs are connected, or by which the graphene sheets act as "bridges" to connect the MWNTs. In either way, the crosslinking improves the electron transfer property by providing more electrical pathways.
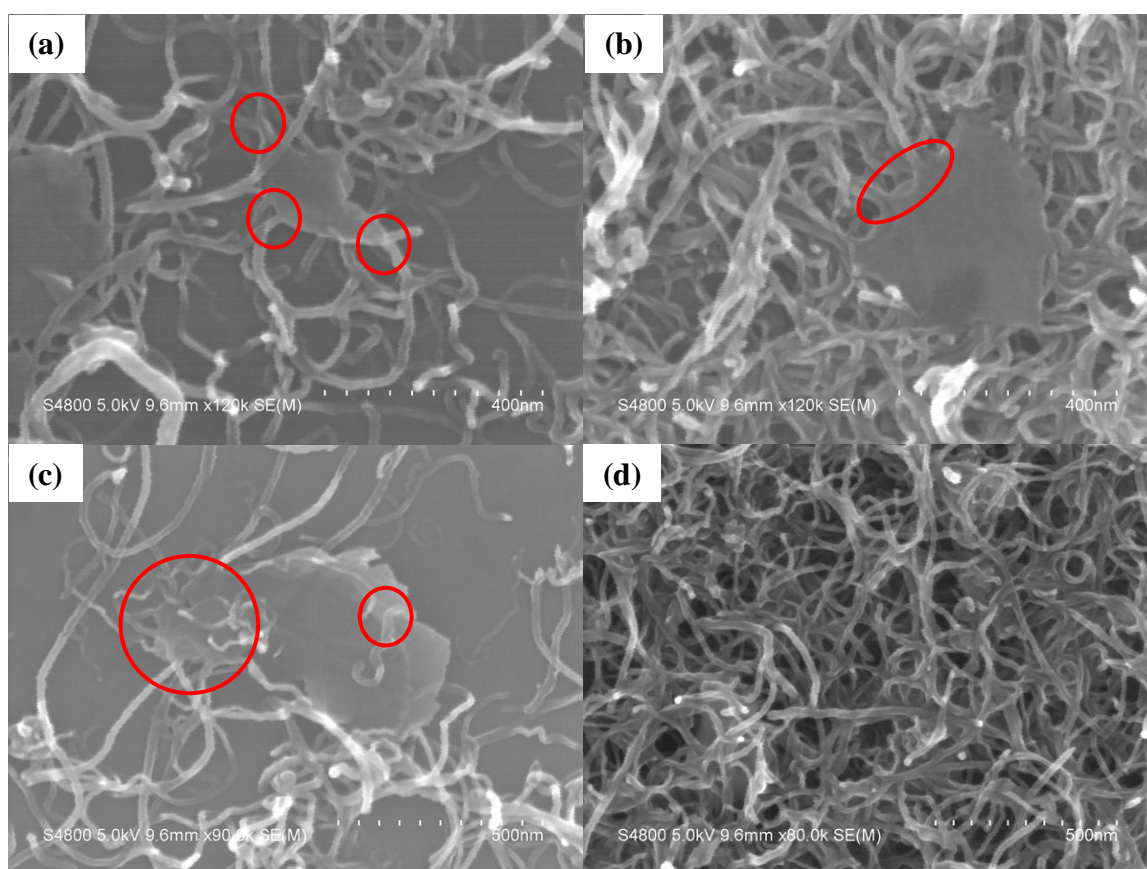
Fig 2.8 SEM images of the composite film, showing crosslinking between ME-LOMWNTs and ME-LOGr.

Although currently, we still do not know the exact mechanism yet, here, we hypothesize that a Fischer esterification reaction has occurred between ME-LOMWNT

and the edge of ME-LOGr sheets (Fig 2.9). It is known that heat is required for a Fischer

esterification reaction, which can be generated by the sonication during the synthesis of

the films. A sonication process creates cavitation bubbles, and the implosion of these

bubbles generates heat, which is spatially localized and temporally transient.[26] With the

generated heat and the amphiprotic water molecule, Fischer esterification occurs between

hydroxyl, epoxide, or carboxylic groups on the ME-LOMWNTs and ME-LOGr sheets.
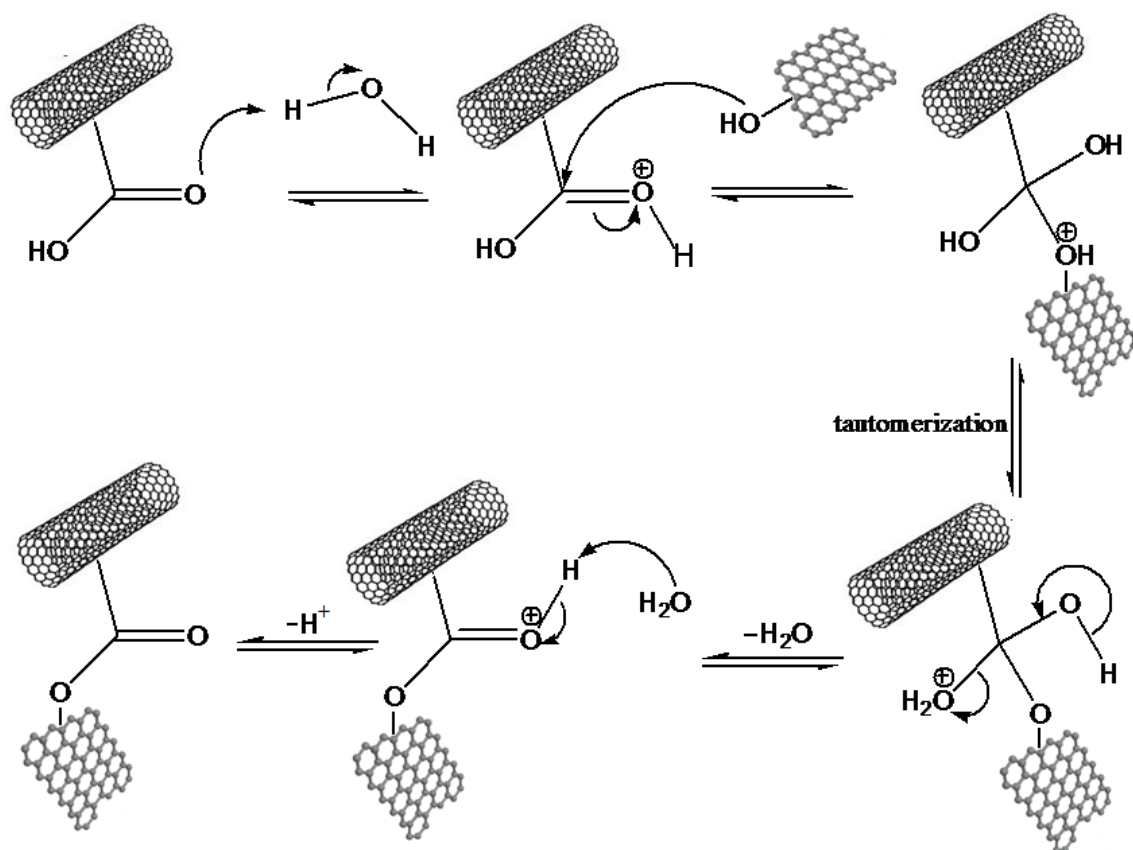
Fig 2.9 Possible mechanism for the crosslinking between ME-LOMWNTs and ME-
LOGr: *Fischer esterification*

Besides esterification, formation of conjugated structure, formation of ether between

hydroxyl groups, and decarboxylation are also possible. For a detailed study on the

mechanism, Fourier transform infrared spectroscopy (FTIR) of the crosslinked solution is

in progress.

2.3.4. Acidic environment to promote crosslink between MWNTs and between graphene sheets

Since the crosslinks play important roles in improving the conductivity of the graphene/carbon nanotube hybrid films, we think the key to further improve the conductivity of the hybrid films is to increase and promote the number of crosslinks. As one of the possible ways, concentrated acidic medium (H_2SO_4) was introduced during the sonication process. We indeed found that that conductivity of the fabricated films is much higher than that of films fabricated by sonication in water.

(a)	**(b)**	**(c)**
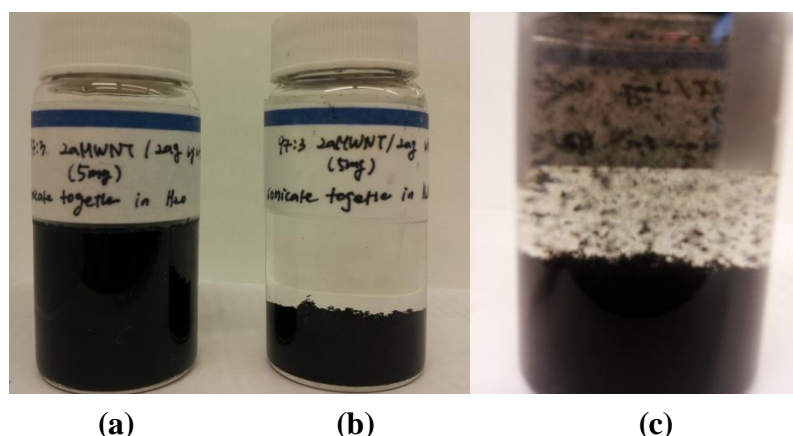
Fig 2.10 Digital photographs of wt% 97/3 (ME-LOMWNTs/ME-LOGr) mixture after 1 hour of bath sonication in: (a)water; (b)in concentrated H_2SO_4; and (c)a photograph of the "fluffy" precipitates in (b).

To easily realize an acidic environment, in this study, the dry products of ME-LOMWNTs and ME-LOGr were mixed, instead of the dispersed suspensions. The mixture of dry products was sonicated in concentrated H_2SO_4 to synthesize composite solutions, which rapidly formed "fluffy" precipitates on the bottom of the vial (Fig 2.10). We hypothesize that the combination of sonication and the concentrated acidic medium

effectively produces heavy crosslinking between ME-LOMWNTs and ME-LOGr, which makes the products to precipitate.

Table 2.1 displays the sheet conductance of the hybrid film formed in the presence of acidic medium, as well as the hybrid film formed in the absence of the acidic medium. In fact, the combination of sonication and acidic medium increased the sheet conductance by a factor of 2.4, from 26,979 S/m to 65,522 S/m. Note that these films are prepared by mixing the dry ME-LOMWNTs and ME-LOGr instead of the dispersed aqueous suspensions. However, this simple change in the procedure led to a significant difference in film conductivity. The conductivity of the film is approximately 9 times lower that of films prepared from the pre-dispersed ME-LOMWNTs and ME-LOGr aqueous suspensions. This dramatic decrease of sheet conductance was resulted because by combing the dry products, it produces a composite solution that is less dispersed. While it is promising that acidic environment indeed promoted crosslinking between tubes and graphene sheets in the films, which resulted in increased conductivity of the films compared to those control films which were sonicated in water.

Wt% 97/3 ME-LOMWNT/ ME-LOGr film by sonication in	Avg Sheet Resistance (Ω/sq)	Avg Sheet Conductance (S/m)	Film Thickness (nm)
Water	124.8	26979	297
H$_2$SO$_4$	117.4	65522	130

Table 2.1 Results of wt% 97/3 (ME-LOMWNTs/ME-LOGr) films formed after 1 hour of sonication in water vs. in concentrated acid, H$_2$SO4.
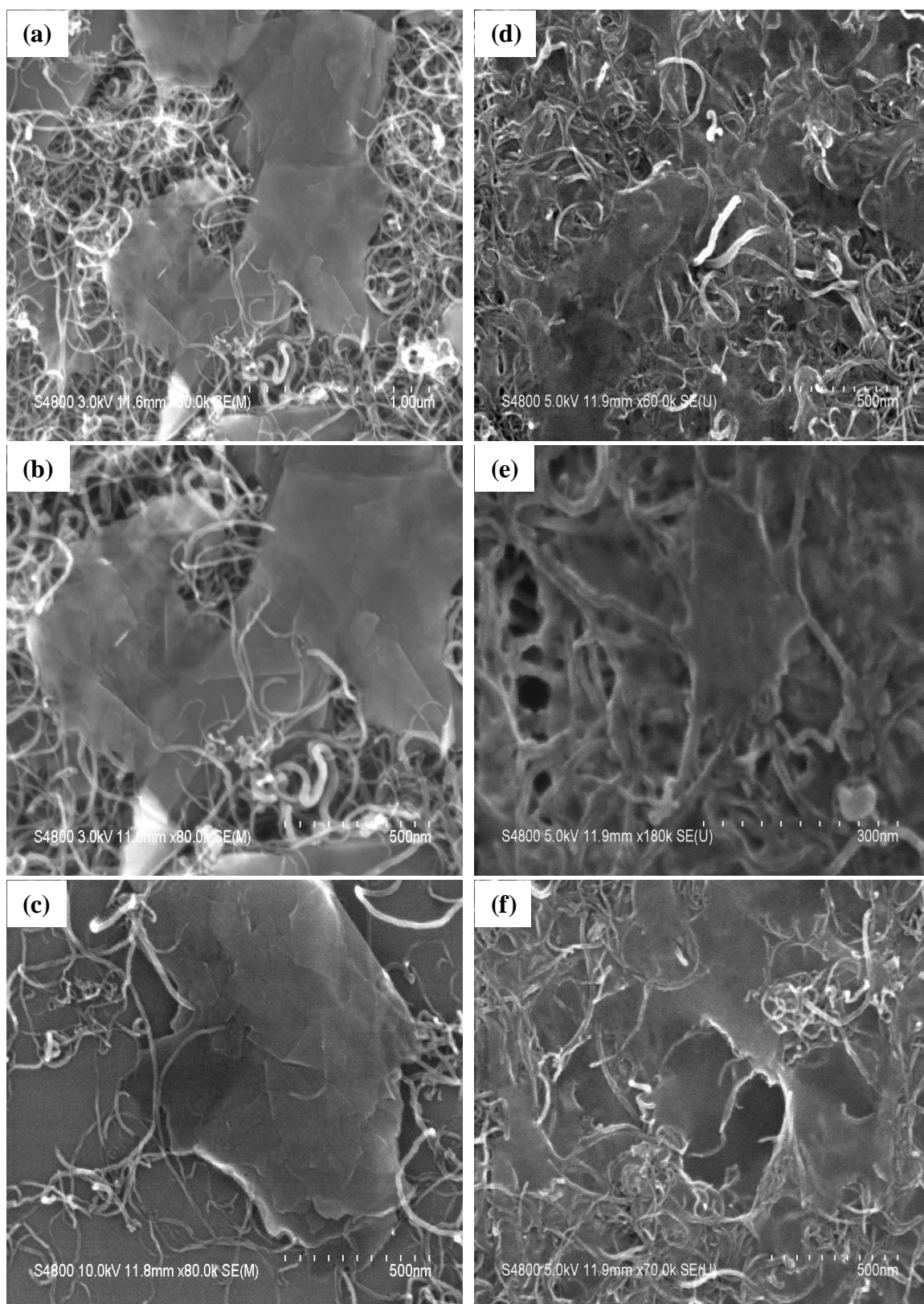
Fig 2.11 SEM images of composite (wt% ME-LOMWNTs/ME-LOGr = 97/3) after 1 hour of bath sonication in: (a)-(c)water, and (d)-(f)concentrated H_2SO_4

We also applied SEM imaging to characterize how the CNTs and graphehe sheets were arranged in the films. In Figure 2.11, the images (d)-(f) represent the films formed in the combination of sonication and acidic medium. They displayed more crosslinks compared to those in the SEM images (a)-(c), which are images of hybrid films in the absence of acidic medium. Additionally, we have mentioned previously that possibly, there are crosslinks between ME-LOMWNTs or between ME-LOGr, which was more apparent (Fig 2.12). The ME-LOMWNTs were crosslinked together that they showed "sheet-like" structures, instead of showing their intrinsic tubular structures.
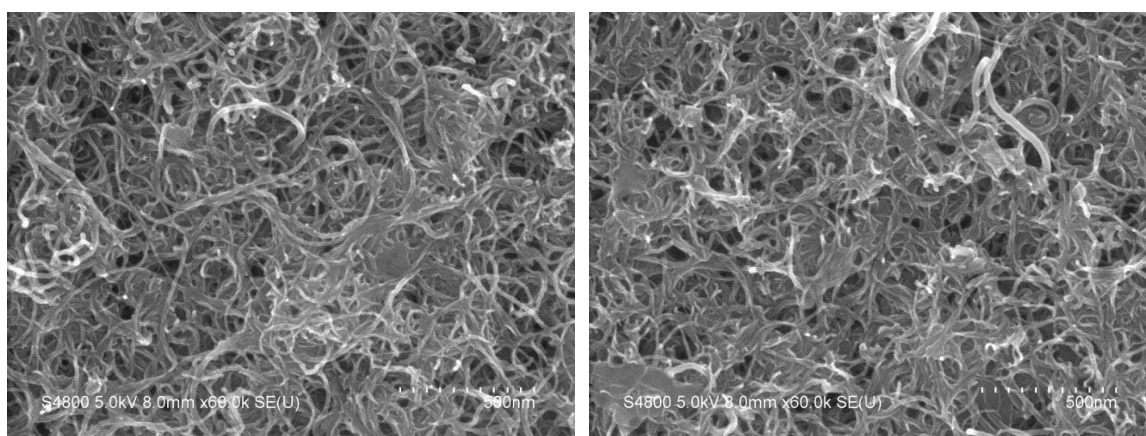
Fig 2.12 SEM images of the composite solution (ME-LOMWNTs/ME-LOGr = 97/3), showing the crosslinks between ME-LOMWNTs.

2.3.5 Raman spectroscopy to characterize the crosslinked films

Raman spectra of both films that were formed with and without acidic environment are shown in Fig 2.13. They displayed similar D-to-G band intensity ratio (I_D/I_G) (Fig 2.13, inset table). However, after scanning 4 different spots, the composite solution formed in the absence of acidic medium was represented by two different groups of spectra, where one group with D band is positioned at 1309 cm^{-1} and another at 1303 cm^{-1}. On the other hand, the composite solution synthesized in the acidic medium showed

D band at 1309 cm^{-1} for all the spots we studied. The explanation behind this feature is not yet clear, but it is possibly due to distribution of the crosslink. The sonication in acidic medium produces films, for which the crosslinks were well distributed across the entire film. In contrast, the crosslinks on the film formed without the acidic medium were isolated, so that the crosslinked and non-crosslinked carbon would have different features in the Raman spectra.
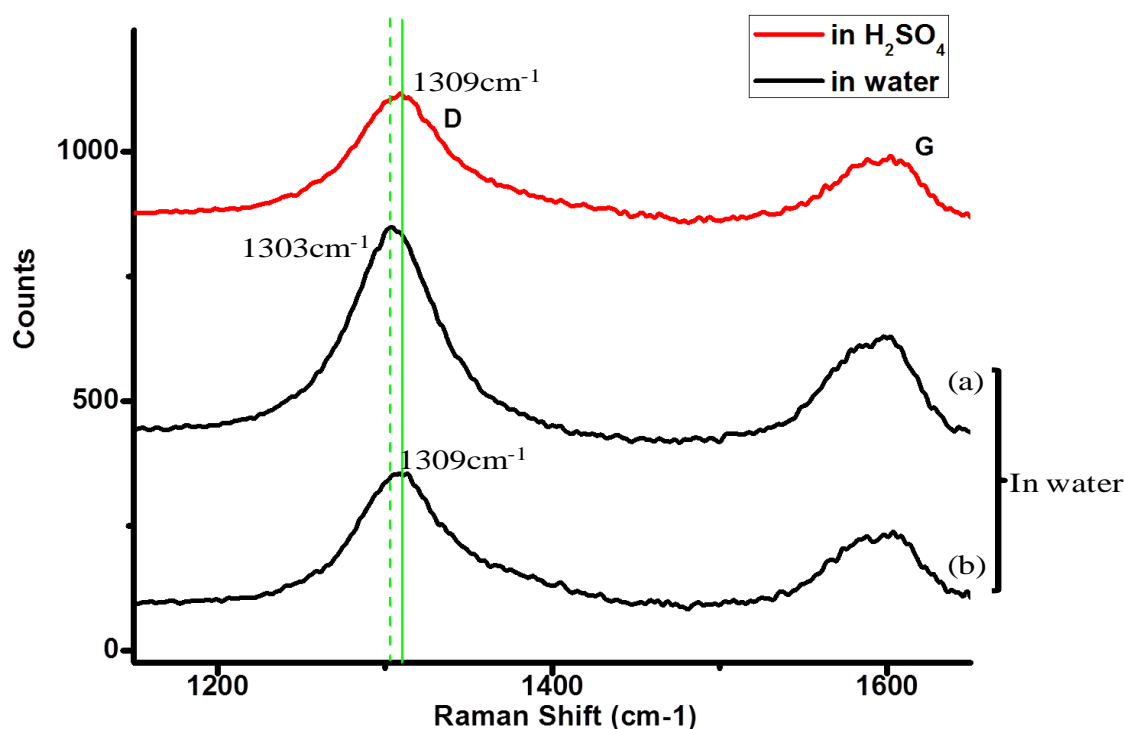
Sample	Intensity of D band (I_D)	Intensity of G band (I_G)	Intensity ratio (I_D/I_G)
In H$_2$SO$_4$	311	185	1.68
In water (a)	548	329	1.66
In water (b)	346	226	1.53

Fig 2.13 Raman spectra of 97/3 ME-LOMWNT/ME-LOGr hybrid film formed with (red) and without (black) acidic environment. Inset table: the D-to-G band intensity ratio (I_D/I_G).
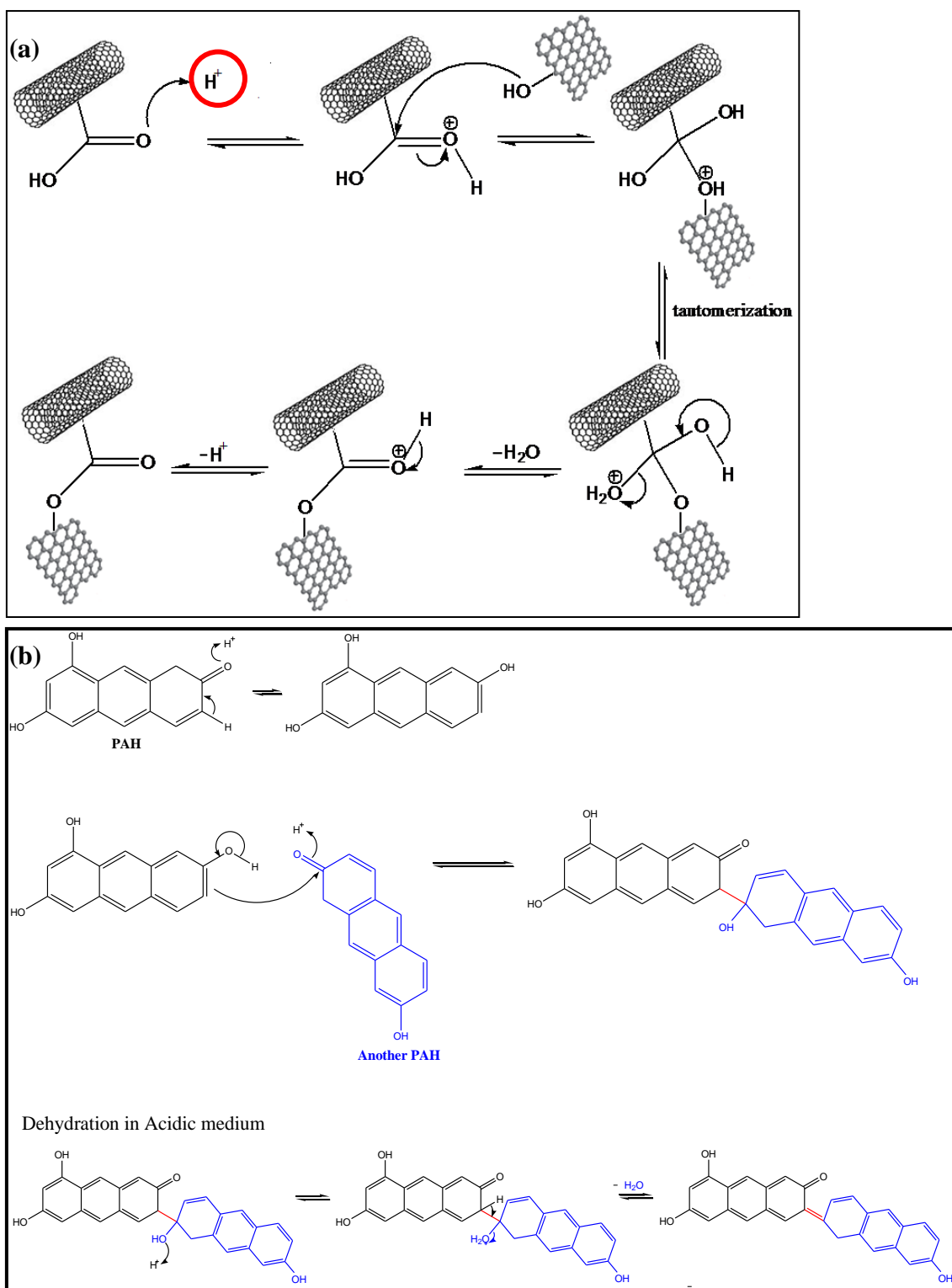
Fig 2.14 Two possible mechanisms for crosslinks of ME-LOMWNTs and ME-LOGr, in combination of sonication and the concentrated acidic medium (H_2SO_4). (a) Acid-catalyzed Fischer esterification; (b)Intermolecular/intramolectural dehydration reactions.

Based on these observations from both SEM and Raman spectroscopy, we formulate two possible mechanisms for the crosslinks formed by the combination of sonication and the concentrated acid (Fig 2.14). The mechanism in Fig 2.14a is similar to the previous Fischer esterification. But, here, the acid was involved instead of the water molecule (indicated by red circle). For the second mechanism (Fig 2.14b), the concentrated acidic medium allows the intramolecular or intermolecular dehydration reactions to form carbon-carbon bonds between ME-LOMWNTs and ME-LOGr by applying Aldol condensation.

2.4   Conclusion

In summary, using our recently developed simple dispersing approach, we directly obtained highly conductive MWNT and graphene aqueous suspensions, which we referred to ME-LOMWNTs and ME-LOGr, respectively. Highly conductive ME-LOMWNTs/ME-LOGr hybrid films on alumina or polycarbonate membranes were fabricated by vacuum filtration. We found that the conductivity of the hybrid films is much higher than that of films made by each of the individual components (MWNTs-only or graphene-only). The increase in conductivity depends on the composition of the hybrids. A weight ratio of 97/3 between MWNTs and graphene reached the highest conductivity of 247,812 S m^{-1}, which is two times higher than that of SWNT/graphene hybrid films reported by Coleman et al.[8] In this work, we also found a very interesting phenomenon that the MWNTs and graphene can be crosslinked, in an acid environment. This crosslinking can be further promoted, which largely contributes to the enhanced conductivity of the hybrid films.

References

[1] S. Iijima, Nature. 1991, **354**, 56.

[2] Lee, S.; Noh, J.H.; Bae, S.-T.; Cho, I.-S.; Kim, J. Y.; Shin, H.; Lee, J.-K.; Jung, H. S.; Hong, K. S. *J Phys. Chem. C* **2009**, 113, 7443-7447.

[3] Liu, X. L.; Han, S; Zhou, C. W. *Nano Lett.* **2006**, 6, 34-39.

[4] Meitl, M. A.; Zhou, Y. X.; Gaur, A.; Jeon, S.; Usrey, M. L.; Strano, M. S.; Rogers, J. A.; *Nano Lett.,* **2004**, 4, 1643-1647.

[5] Snow, E. S.; Campbell, P.M.; Ancona, M. G.; Novak, J. P. *Appl. Phys. Lett.,* **2005,** 86, 033105-1-033105-3.

[6] Bradley, K.; Gabriel, J. C. P.; Gruner, G. *Nano Lett.,* **2003,** 3, 133-1355.

[7] Saran, N.; Parikh, K.; Suh, D. S.; Munoz, E.; Kolla, H.; Manohar, S. K. *J. Am. Chem. Soc.,* **2004,** 126, 4462-4463.

[8] Tung, V.C.; Chen, L. M.; Allen, M. J.; Wassei, J. K.; Nelson, K.; Kaner, R. B.; Yang, Y. Nano Lett. **2009**, 9, 1949-1955.

[9] Hong, T.-K.; Lee, D. W.; Choi, H. J.; Shin, H. S.; Kim B.-S. *ACS Nano*. **2010**, 4, 7, 386-3868.

[10] Chiu, P. L.; Mastrogiovanni, D. D. T.; Wei, D.; Louis, C.; Jeong, M.; Yu, G.; Saad, P.; Flach, C. R.; Mendelsohn, R.; Garfunkel, E.; He, H. *J. Am. Chem. Soc.,* **2012**, 134, 5850

[11] Wang, S.; Tang, L.A.; Bao, Q.; Lin, M.; Deng, S.; Goh, B.M.; Loh, K.P. *J. Am. Chem. Soc.,* **2009**, 131, 16832-16837.

[12] Tung, V. T.; Allen, M. J.; Yang, Y.; Kaner, R. B. *Nature Nanotech.* **2009**, *4*, 25.

[13] Li, D.; Muller, M. B.; Gilje, S.; Kaner, R. B.; Wallace, G. G. *Nature Nanotechnology* **2008**, *3*, 101.

[14] Hernandez, Y.; Nicolosi, V.; Lotya, M.; Blighe, F. M.; Sun, Z. Y.; De, S.; McGovern, I. T.; Holland, B.; Byrne, M.; Gun'Ko, Y. K.; Boland, J. J.; Niraj, P.; Duesberg, G.; Krishnamurthy, S.; Goodhue, S.; Hutchison, J.; Scardaci, V.; Ferrari, A. C.; Coleman, J. N. *Nature Nanotech.* **2008**, *3*, 563.

[15] Becerril, H. A.; Mao, J.; Liu, Z. F.; Stoltenberg, R. M.; Bao, Z.; Chen, Y. S. *ACS Nano* **2008**, *2*, 463.

[16] Taft, E. A.; Philipp, H. R. *Phys. Rev.* **1965**, *138(1A)*, A197.

[17] Marinopoulos, A. G.; Reining, L.; Olevano, V.; Rubio, A.; Pichler, T.; Liu, X.; Knupfer, M.; Fink, J. *Physical Review Letters* **2002**, 89.

[18] Kelly, M. K.; Etchegoin, P.; Fuchs, D.; Kratschmer, W.; Fostiropoulos, K. *Physical Review B* **1992**, *46*, 4963.

[19] Marinopoulos, A. G.; Wirtz, L.; Marini, A.; Olevano, V.; Rubio, A.; Reining, L. *Applied Physics a-Materials Science & Processing* **2004**, *78*, 1157.

[20] Marinopoulos, A. G.; Reining, L.; Rubio, A.; Vast, N. *Physical Review Letters* **2003**, 91.

[21] Marinopoulos, A. G.; Reining, L.; Rubio, A.; Olevano, V. *Physical Review B* **2004**, 69.

[22] Kramberger, C.; Hambach, R.; Giorgetti, C.; Rummeli, M. H.; Knupfer, M.; Fink, J.; Buchner, B.; Reining, L.; Einarsson, E.; Maruyama, S.; Sottile, F.; Hannewald, K.; Olevano, V.; Marinopoulos, A. G.; Pichler, T. *Physical Review Letters* **2008**, *100*.

[23] Yoo, S.; Jung, Y. M.; Lee, D. S.; Han, W. T.; Oh, K.; Murakami, Y.; Edamura, T.; Maruyama, S. *Optics Letters* **2005**, *30*, 3201.

[24] Murakami, Y.; Einarsson, E.; Edamura, T.; Maruyama, S. *Physical Review Letters* **2005**, *94*.

[25] Murakami, Y.; Einarsson, E.; Edamura, T.; Maruyama, S. *Carbon* **2005**, *43*, 2664.

[26] Bang, J. H.; Suslick, K. S. *Adv. Mater.* **2010**, 22, 1039-1059.

CHAPTER 3   Fabrication of 1D-Nanotube/2D-Graphene Hybrid Film by Interfacial Self-Assembly

3.1   Introduction

A facile and fast filtration approach was performed to fabricate all the films in the previous chapter. However, there are some limitations to this approach. While the fabricated films are relatively conductive, they are not transparent, which limits their applications such as transparent electrodes. Additionally, the film needs to be transferred to a substrate for practically applications. Such transfer process has been introduced by Jung and co-workers.[1] Using a specially designed process, they have successfully transferred a layer-by-layer assembled graphene and gold nanoparticle hybrid film that they prepared by vacuum filtration, onto quartz substrate. However, the film size is limited to the size of filter member. Also, the process itself is very time-consuming and inefficient. These disadvantages of the transfer process are critical issue for industrial use, where it requires production of large quantities of high quality films within short period of time. Therefore, a solution to these disadvantages is needed for the filtration approach to be effective and practical.

While the solution is not yet discovered, there have been extensive studies to develop an alternative method to assemble nanomaterial films, such as Langmuir-Blodgett (LB) deposition,[2,3] layer-by-layer sequential adsorption,[4,5] spin-coating,[6,7] ultrasonic adsorption,[8,9,10,11] solvent evaporation,[12,13] and covalent attachment.[14,15,16,17] However, these approaches also require special apparatus, and they are time-consuming and limited only to some nanomaterials.[18]
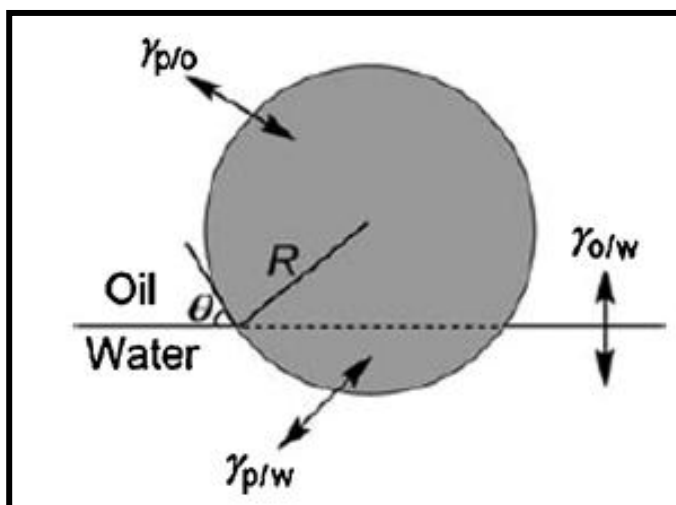
Fig 3.1 Schematic representation that demonstrates the interfacial tensions between the particle and oil ($\gamma_{p/o}$), the particle and water ($\gamma_{p/w}$), the oil and water ($\gamma_{o/w}$) of a nanoparticle. Reproduced from *Angew. Chem. Int. Ed.,* 2010, 49, 10052.

Recently, interfacial self-assembly has received great attention because it is facile and fast approach to prepare films for wide range of nanomaterials, without requiring any special apparatus. Due to its advantages, it has a broad range of applications, such as thin-film capacitors and transistors,[19] solar cell,[20] and high-performance display units.[21,22] The key to self-assembly nanomaterials at liquid-liquid interface is the reduction of interfacial free energy of the system. In oil-to-water system, as the particles move from aqueous phase to the oil-to-water interface, the initial interfacial energy between oil and water partially changes to energy between particles and oil and between particles and water.[23] This change in total interfacial energy ($\Delta\mu$) can be represented by following equation: $\Delta\mu=A(\gamma_{P/W}-\gamma_{P/O}-\gamma_{O/W})$, where A is surface area of the nanoparticles, and $\gamma_{P/W}$, $\gamma_{P/O}$, $\gamma_{O/W}$ are the interfacial tension between particles and water, particles and oil, and oil and water, respectively (Fig 3.1). The interfacial tension between particle and water ($\gamma_{P/W}$) dramatically decreases and the interfacial tension between particle and oil ($\gamma_{P/O}$) increases, so that the self-assembly at the interface is attributed by the negative total interfacial

energy change. The first attempt to apply the interfacial self-assembly to nanoparticles was performed by Vanmaekelbergh and co-workers.[24] They self-assembled a 2D monolayer of charged gold nanocrystals at the oil-water interface with a help of inducer, ethanol. They reported that ethanol reduces the charge density on the particles, which reduces the total interfacial energy and therefore promotes the self-assembly.[24] Miyashita and co-workers also used ethanol as inducer for a multi-walled nanotube (MWNT) film fabrication.[25] They proposed that the surface charge of the MWNTs is decreased as the negatively charged carboxyl anions at the MWNT surfaces form hydrogen bonds with the hydroxyl groups of ethanol (Fig 3.2).[25] More recently, the interfacial self-assembly of graphene oxide (GO) at the oil-water interface was studied.[23] In this work, they employed the high affinity property of GO at the interface to use them as surfactants in Pickering emulsion polymerization to fabricate graphene-based polymer composites.[23]
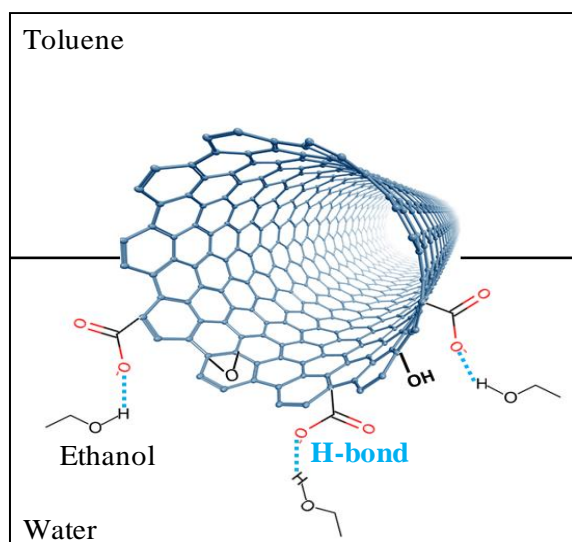
Fig 3.2 Schematic representation of carbon nanotube at toluene-water interface.

Likewise, there have been extensive studies and efforts to use the interfacial self-assembly to effectively produce nanomaterial films for a variety of applications. Yet, not many studies were reported on fabrication of nanotubes/graphene hybrid film using this process. In the present study, we use the interfacial self-assembly to fabricate ME-

LOMWNTs/ME-LOGr hybrid film and compare with the hybrid film that we have fabricated using vacuum filtration method described in the previous chapter. Within this work, our new focus was on the structure of the nanomaterials, because the hybrid film that we fabricated contained two nanomaterials with different dimensionalities. Graphene is an atomically thin 2D structure, while MWNT is a typical 1D nanomaterial. Since they contain different structural dimensions, we study how these two nanomaterials behave differently at the interface. Here, we use interfacial self-assembly to fabricate a hybrid film of 2D graphene and 1D MWNTs.

3.2   Experimental procedure

3.2.1   Chemicals

Graphite powder (~20 μm) was purchased from Sigma Aldrich and used as received. Multi-walled nanotube powder was received from China and also used as received. ACS grade concentrated sulfuric acid (98% H_2SO_4) and concentrated nitric acid (70% HNO_3) were purchased from Pharmco-AAPER and used as received. ACS certified sodium hydroxide pellets were purchased from Fisher Scientific. Argon, high purity airgas, was used for perching. Deionized water (18.2 MΩ) (Nanopore water, Barnstead) was used to prepare all solutions, as well as to rinse and clean the samples.

3.2.2 Fabrication of the hybrid film on quartz/glass substrate by vacuum filtration and transfer
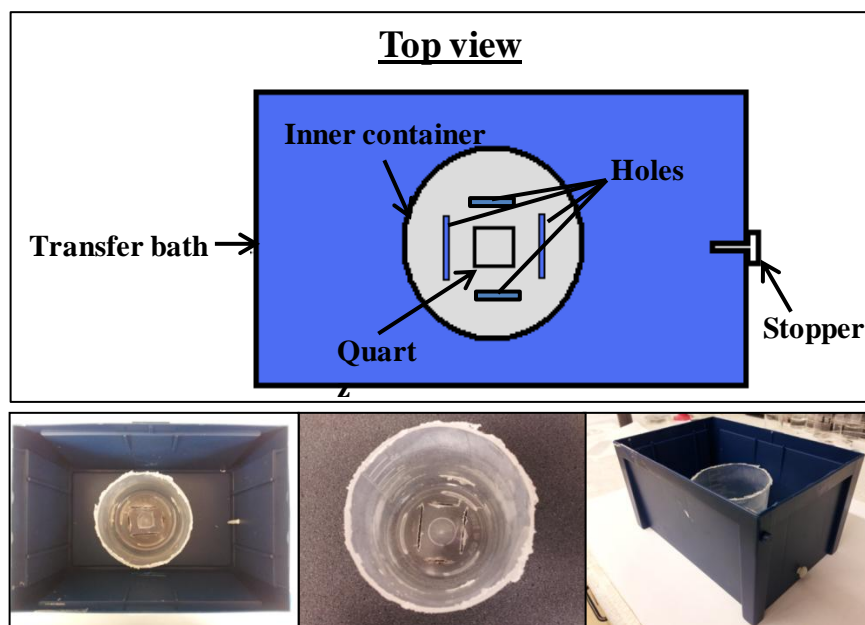
Fig 3.3 Schematic drawing and digital photographs of transfer apparatus for the composite film prepared by filtration approach

ME-LOMWNTs/ME-LOGr hybrid films were fabricated by vacuum filtering the composite solutions through an Anodisc aluminum oxide membrane (0.2 μm pore size, Whatman Ltd.), followed by drying in an oven (80°C) for 2 hours. A special apparatus (Fig 3.3) was required to transfer the film onto a substrate, such as glass or quartz. First, the substrate was placed on the bottom of inner container. The inner container with the substrate on the bottom was placed in a transfer bath, and the bath was filled with 1M NaOH. Inside the inner container, the hybrid film with the alumina membrane was carefully placed on the surface of the NaOH solution. After certain period of time, the alumina membrane was etched away and only the hybrid film was floated on the surface of NaOH solution. Then, the stopper was removed and the NaOH solution was diluted by recirculation with water. The recirculation was performed very slowly and carefully, so

that the floating film was not disrupted. The recirculation process was continued until the

pH of the bath reached 7. When the pH reached 7, the water was slowly drained out until

the floating hybrid film was attached to the substrate. Then, the film on the substrate was

dried in an oven (80°C) for 12 hours. We refer to the obtained films as filtered-films.

3.2.3   Fabrication of the hybrid film by interfacial self-assembly
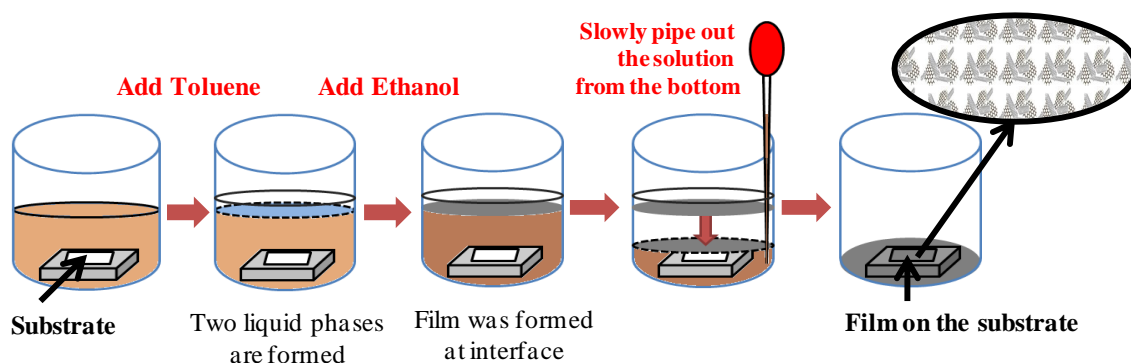
Fig 3.4 Schematic illustration of interfacial self-assembly procedure

Figure 3.4 demonstrates the schematic illustration of overall interfacial self-assembly

procedure for film fabrication. A substrate, such as glass, was placed on the top of a

support that was on the bottom of a container. 8 mL of the composite solution was added

in the beaker. Then, 2 mL of toluene was added to form toluene-to-water interface. An

inducer, ethyl alcohol, was slowly added until a thin uniform film was formed at the

interface. During the addition of the ethanol, occasionally, the solution was gently

bubbled with a pipet to speed up the interfacial assembly process. When a uniform film

was formed at the toluene-to-water interface, the water was slowly pipette out from the

bottom of the beaker until the film at the interface 'sits' onto the glass. The film on the

glass was then dried in an oven (~80 °C) for 12 hours. We refer to these films as

interfacial self-assembled films.

3.2.4 Post-heat treatment

3.2.4a Furnace heating
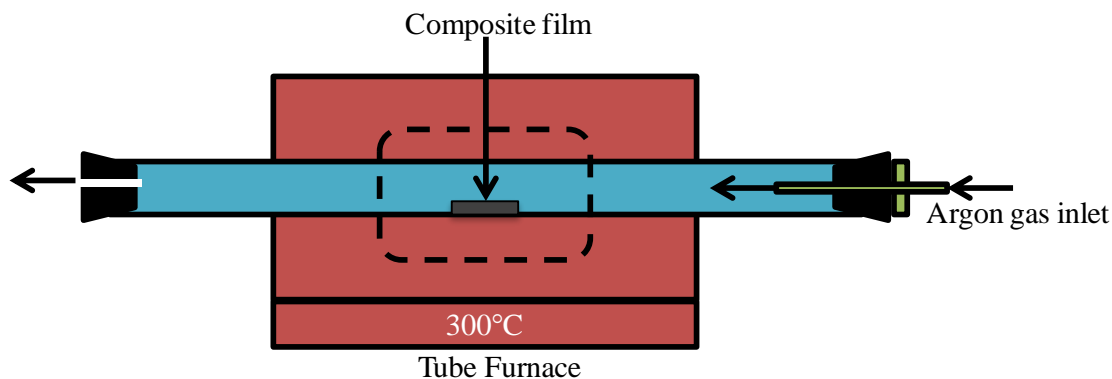
Fig 3.5 Schematic illustration of tube furnace heating apparatus

Sheet resistance of the filtered-films on glass was measured using a manual four-point

resistivity probe (Lucas Laboratories, model 302) before any heat treatment. After the

measurement, the film was placed in the middle of a tube that is made of quartz. Then,

the tube that contains the film was placed inside Tube Furnace (Lindberg/Blue) so that

the middle section of the tube can be heated. One end of the tube was closed with a

stopper, while another end of the tube was connected to inlet of argon gas with flow rate

of 40 mL/min (Fig 3.5). The system was perched with the inert argon gas for an hour to

prevent contact with oxygen. Then, the furnace was set at 300°C and the film was heated

for an hour. After the hour, the system was slowly cooled down to room temperature.

When the system was near the room temperature, the film was taken out from the tube,

and sheet resistance was measured. Using the same parameters, the film was heated in the

furnace for additional 2 hours. Then, sheet resistance of the film was measured again.

The interfacial self-assembled films on glass substrates were thermally treated with the

same manner as the filtered films. Before any heat treatment, sheet resistance of the films

were measured using the four-point probe, and film transmittance was measured using a

Cary 500 Ultraviolet-visible-near-infrared spectrophotometer. The films were first heated

for an hour at 300°C, then additional 2 hours at 300°C, followed by another hour at

500°C. Sheet resistance and transmittance of the films were measured after each cycle of

heat treatment.

3.2.4b Microwave heating
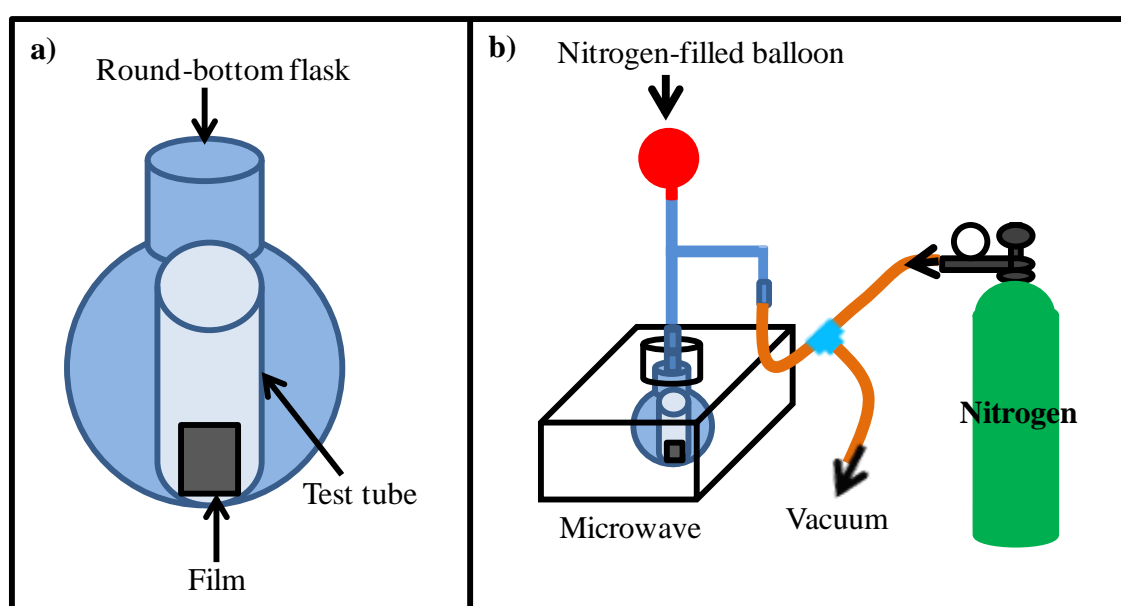
Fig 3.6 Schematic illustration of microwave heating apparatus

Sheet resistance of a transferred filtered-film on quartz was measured using a manual

four-point resistivity probe (Lucas Laboratories, model 302) before any heat treatment.

After the measurement, the film was placed inside a test tube, and the test tube was

placed inside a round-bottom flask (Fig 3.6a). Then, the round-bottom flask was placed in

the microwave reactor (CEM-Discover). The system was perched with nitrogen gas and

vacuum, alternately, for 15 times to prevent contact with oxygen. The microwave heating

was performed in inert atmosphere with nitrogen gas. With a fixed microwave-power at

200W, the film was heated with microwave duration of: 5 seconds, 10 seconds, 10

seconds, and 20 seconds. Sheet resistance of the film was measured after each cycle of

heating.

3.2.5   Characterizations and measurements

3.2.5a Electrical property of hybrid films

For different ratio composite solutions, UV-vis-NIR absorption spectra of wavelength

ranging 200nm to 800nm were obtained using a Cary 500 Ultraviolet-visible-near-

infrared spectrophotometer in double-beam mode. For interfacial self-assembled films on

glass substrate, sheet resistances were measured using a manual four point resistivity

probe (Lucas Laboratories, model 302). For the conductivity comparison with the

filtered-films, the measurements of the hybrid films on polycarbonate track-etch filter

membrane (0.22 μm pore size; Millipore) from previous chapter were used. Since the

polycarbonate filter membrane melts/burns at high temperature, the transfer process

described in 3.2.2 was required for the filtered-films. Sheet resistance of the films was

measured before and after the transfer. During heat treatment, sheet resistance of the

hybrid films was measured after each cycle of heat treatment.

3.2.5b Scanning electron microscope

For characterizing the composite solutions, SEM samples were prepared by depositing

the solution onto a SiO_2/Si substrate. The substrate was first cleaned in piranha solution

for 15 minutes, followed by 15 minutes in water using bath sonication. For comparison

between the filtered-films and the interfacial self-assembled films, SEM samples of

filtered-films were prepared by filtering each composite solution through an Anodisc

with support disk, aluminum oxide anopore membrane (0.2 μm pore size; Whatman Ltd.)

and drying it in an oven (~80°C) for 2 hours. Meanwhile, SEM samples for the interfacial

self-assembled films were prepared during the film fabrication by substituting glass

substrate with SiO_2/Si substrate. High contrast SEM images of the hybrid films with

different ratio of ME-LOMWNT and ME-LOGr were obtained using a Hitachi S-4800

field emission scanning electron microscope (FE-SEM, Hitachi Co. Ltd. S-4800) under

small accelerating voltage (1-2 KV) and a high probe current (15-20 μA).

3.2.5d Atomic force microscopy (AFM)

The thickness of the hybrid films was measured using a Nanoscope IIIa multimode SPM

(Digital Instrument) with a J scanner operated in "Tapping Mode". For AMF samples, the

self-assembled hybrid films on the glass substrates were used as transferred. A 160 μm

long rectangular silicon cantilever/tip assembly (Model: MPP-12100, Veeco) with a

resonance frequency of 160 kHz, a spring constant of 7.7 N/m, and tip radius of less than

10nm was used for imaging. The scanning was performed at a rate of ~0.7 Hz. The

thickness of the films was obtained by measuring average height difference between film

and bare filter membrane from section analysis of the topographic images.

3.2.5e Thermogravimetric Analysis (TGA)

Using a Perkin Elmer Thermogravimetric Analyzer Pyris 1 TGA, the analysis was

formed on sample sizes of about 2-3 mg with a nitrogen flow of 20 mL/min. At a rate of

5 °C/min, the samples in the TGA furnace were heated from room temperature to 1000

°C, as the mass was recorded as a function of temperature.

3.3   Results and discussion

3.3.1   Interfacial self assembly of 1D multi-walled carbon nanotubes, atomically thin 2D graphene sheets, and their mixture

The suspensions of ME-LOMWNTs/ME-LOGr with different weight ratio for the

study of interfacial self-assembly were prepared in the same manner as before, combining

the ME-LOMWNT solution and ME-LOGr solution, followed by bath sonication for 1

hour. First, we studied on behavior of two different dimensional nanomaterials (1D

MWNT and 2D graphene) at the oil-to-water interface. Each solution of ME-LOMWNT

(1D) and ME-LOGr (2D) was prepared in a vial. The ME-LOGr solution was

approximately 10 times concentrated than the ME-LOMWNT solution. As 1 mL (12.5%)

of ethanol was added to each vial, the thin films of both ME-LOGr and ME-LOMWNT

were assembled at the toluene-to-water interface (Fig 3.7a and d, respectively). The

closer observations of the films indicated that the ME-LOMWNT film contained very

small amount of aggregates within the film, while ME-LOGr film was uniform and stable

(Fig 3.7e and b, respectively) The ME-LOGr film remained stable with additional volume

of ethanol (2 mL, 25 vol%). However, amount of 3D aggregates in ME-LOMWNT film

increased (Fig 3.7d-f) that it formed a highly aggregated film at the interface. When

excess amount of ethanol (5 mL, 62.5 vol%) was added to the ME-LOGr solution, the

film cracked and formed isolated "islands" of the films. Yet, no 3D aggregates were

observed (Fig 3.7c). After they were left at room temperature for one day, some

precipitations were observed on the bottom of ME-LOMWNT vial. As Miyashita and co-workers reported, MWNTs form 3D aggregates with excessive amount of ethanol by hydrophobic interactions and/or π-π interactions during the assembly.[25] The absence of the aggregates in the ME-LOGr film indicated that ME-LOGr tends to self-assemble a more stable film than ME-LOMWNT. Its ability to form more stable film possibly demonstrates that the ME-LOGr has a higher affinity to both water and oil phases that it spontaneously adsorbed at the interface to form the stable film.
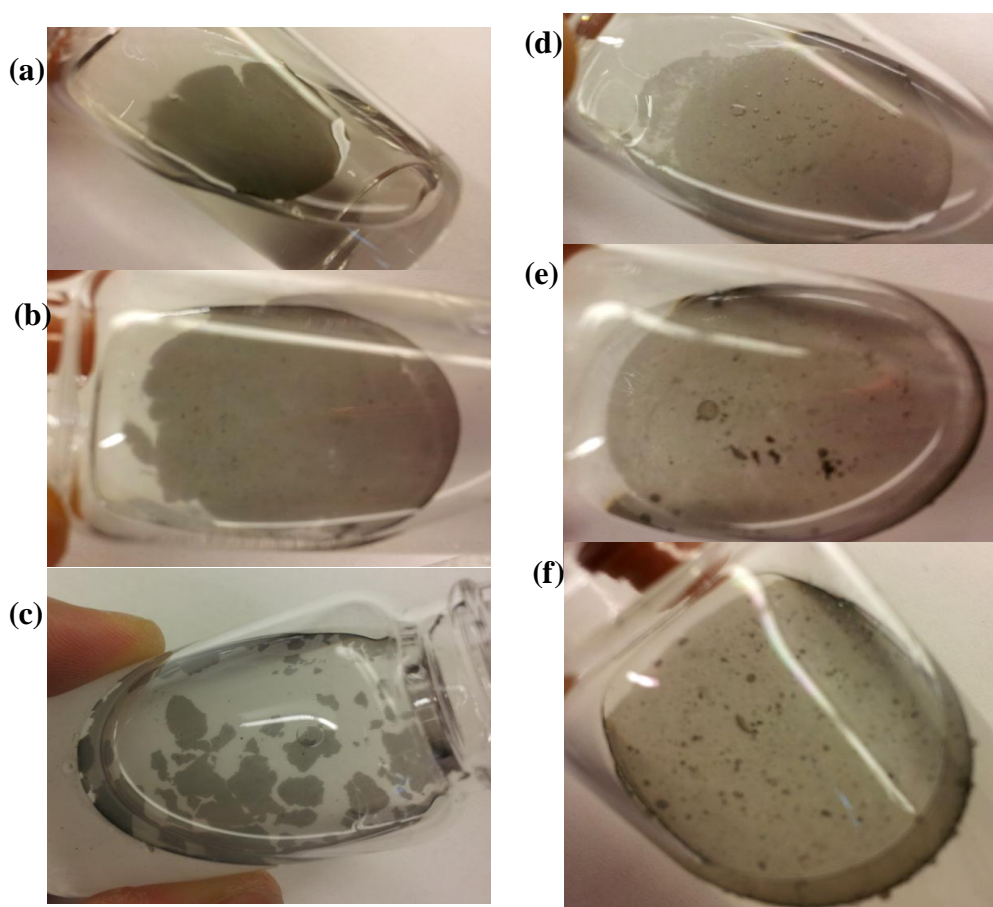
Fig 3.7 Digital photographs of: ME-LOGr-only (a)-(c) and ME-LOMWNT-only solutions (d)-(f) with mL, 2mL,5mL ethanol, respectively
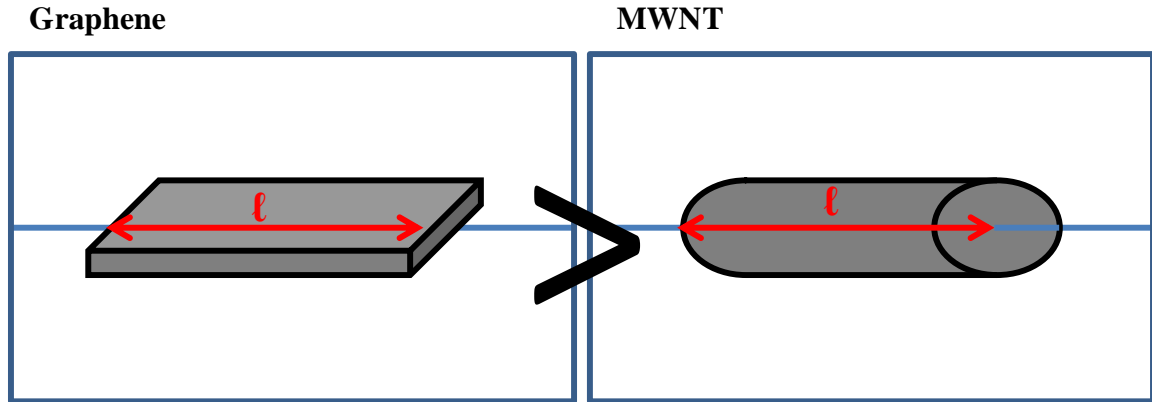
Graphene   **MWNT**

Fig 3.8 Schematic illustration of surface area of graphene and MWNT at the interface.

Also, according to the equation that was previously described, $\Delta\mu=A(\gamma P/W-\gamma P/O-\gamma O/W)$, the surface area of the sheet at the interface is another contributor to determine the total change of interfacial energy in the system. Graphene, ME-LOGr, is a 2D one atomically thin layer structure. Even though it is not clear how this atomically thin layer of graphene forms at the interface,[23] we believe that within the same length, the graphene sheet contains large surface area at the interface relative to the MWNTs, a 1D cylindrical nanostructure (Fig 3.8). When $\gamma_{O/W}$ is greater than $\gamma_{P/W}-\gamma_{P/O}$, the self-assembly at the interface is more favorable for the particles with larger surface area. There, with our assumption of graphene sheets generally having greater surface area, the self-assembly of graphene should be more favorable than that of MWNTs. The self-assembled ME-LOMWNT-only and ME-LOGr-only films behave differently at interface because of the different interfacial energy due to the different shape of the nanostructures.
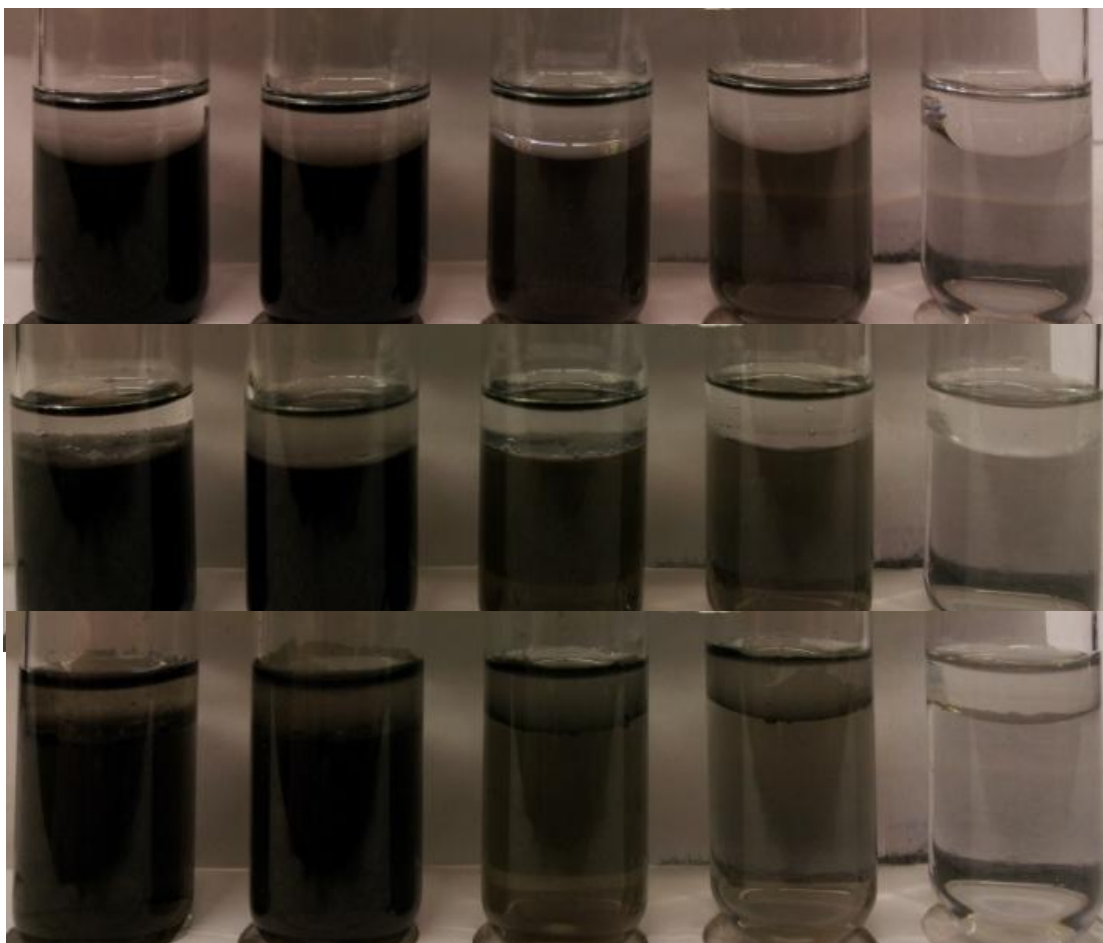
Fig 3.9 Digital photographs of the ME-LOMWNT/ME-LOGr composite solutions:
(a) before adding ethanol, (b) after adding 0.25 mL (~4%) ethanol, and (c) after
adding 0.75 mL (12.5%) ethanol

With this observation at mind, the composite solutions with different ratio of ME-

LOMWNT and ME-LOGr (ME-LOMWNTs/ME-LOGr: 100/0, 97/3, 75/25, 25/75, and

0/100) were prepared to assemble graphene/MWNT hybrid films at the interface (Fig 3.9).

The weight of the carbon nanomaterials (ME-LOGr and ME-LOMWNTs) was kept

constant for all the solutions. As each film was assembled at the interface, we observed

that the suspension with more ME-LOGr content tended to form a lighter-colored,

uniform, and stable film at the interface, compared to that with more ME-LOMWNT

contents. Also, the composite solution with more MWNT contents tended to aggregate

more, which produced the highly aggregated film. This result was consistent with the

previously observed results, where we prepared graphene-only and MWNTs-only films,

and observed that MWNTs are more tended to form aggregates in the film.

3.3.2. Development of a new and simple film transfer method

The self-assembled films at the oil-to-water interface are required to be

transferred to substrates for practical device applications and their conductivity study.

However, in literatures, the transferring process was performed by slowly immersing a

substrate into the solution, and then pulling it out by horizontal or vertical lift as the self-

assembled film at the interface is attached to the substrate.[1] The method is facile and

suitable for almost any substrates. Yet, this method often requires a modification of

substrate, in order for films to have strong affinity so that they can be attached to the

substrate. In addition, this transfer method often tends to destroy the uniformity of the

assembled film at the interface, because some parts of the film at the interface are

attached to the substrate during the substrate immerging, while other parts of the film are

attached during the substrate pulling process. To prevent these disadvantages of the

reported transfer method, we have developed a new method to transfer the film at the

interface onto a substrate. In our transfer method, we slowly pipette out water phase from

the bottom of the vial so that the film at the interface was slowly descended and attached

to the immerged substrate. This method does not require any modification of the substrate

and it fabricates a relatively uniform film since the entire film can reach the substrates at

the same time and then "sits" on the substrate as it has been formed at the interface.

3.3.3 Conductivity measurement of the transferred films: comparison between filtered films and interfacial self-assembled films

ME-LOMWNT/ ME-LOGr	Substrate Type	Avg Film Resistance (kΩ/□)	Avg Film Conductance (S/m)	Avg Film Thickness (nm)	Film Transmittance (%T)
100/0	Glass	4.30	2610	89.1	60.9
	Silicon	4.82			
97/3	Glass	3.23	3630	85.3	59.9
	Silicon	2.58			
75/25	Glass	9.65	1380	75.1	75.8
	Silicon	7.46			
25/75	Glass	8.98	1740	64.0	81.5
	Silicon	11.60			
0/100	Glass	73.3	155	88.0	56.8
	Silicon	46.1			

Table 3.1 Hybrid films by interfacial self-assembly: sheet conductance, film thickness, and film transmittance

After the composite films were formed using interfacial self-assembly, sheet resistance was measured with a four-point resistivity probe and the film thickness was measured by AFM (Table 3.1). We found that the films fabricated by interfacial self-assembly were typically thinner (more than twice) than the films fabricated by filtration approach. Also, unlike the filtered-films, which were opaque films, the self-assembled films were relatively transparent (ranged from 55~80 %T, Table 3.1). Unfortunately, sheet conductance of the self-assembled films was much lower than the filtered-films. Comparing the films with highest conductance from each approach, which was fabricaeded with a ratio of 97/3 for both approaches, sheet conductance of the filtered-films was more than 100 times higher than that of the self-assembled films.

3.3.4 Characterization of the films with scanning electron microscopy

In order to study the morphology of the film using SEM, the assembled films at the oil-to-water interface was transferred onto a conductive substrate, such as a highly doped Si substrate. Figure 3.10 shows the SEM images of the films deposited on a SiO_2/Si substrates using interfacial self-assembly with this new transfer method. As stated earlier, the self-assembled hybrid films were much less conductive than the filtered-films. Possibly, the films formed by interfacial self-assembly have larger distance between tubes or between tubes and graphene sheets than the filtered-films, since the interfacial self-assembly has no external force applied during the fabrication of films.[26] The shown SEM images of the self-assembled films partly support our statement that the self-assembled films have a larger distance between the nanomaterials that leads to a low sheet conductance.
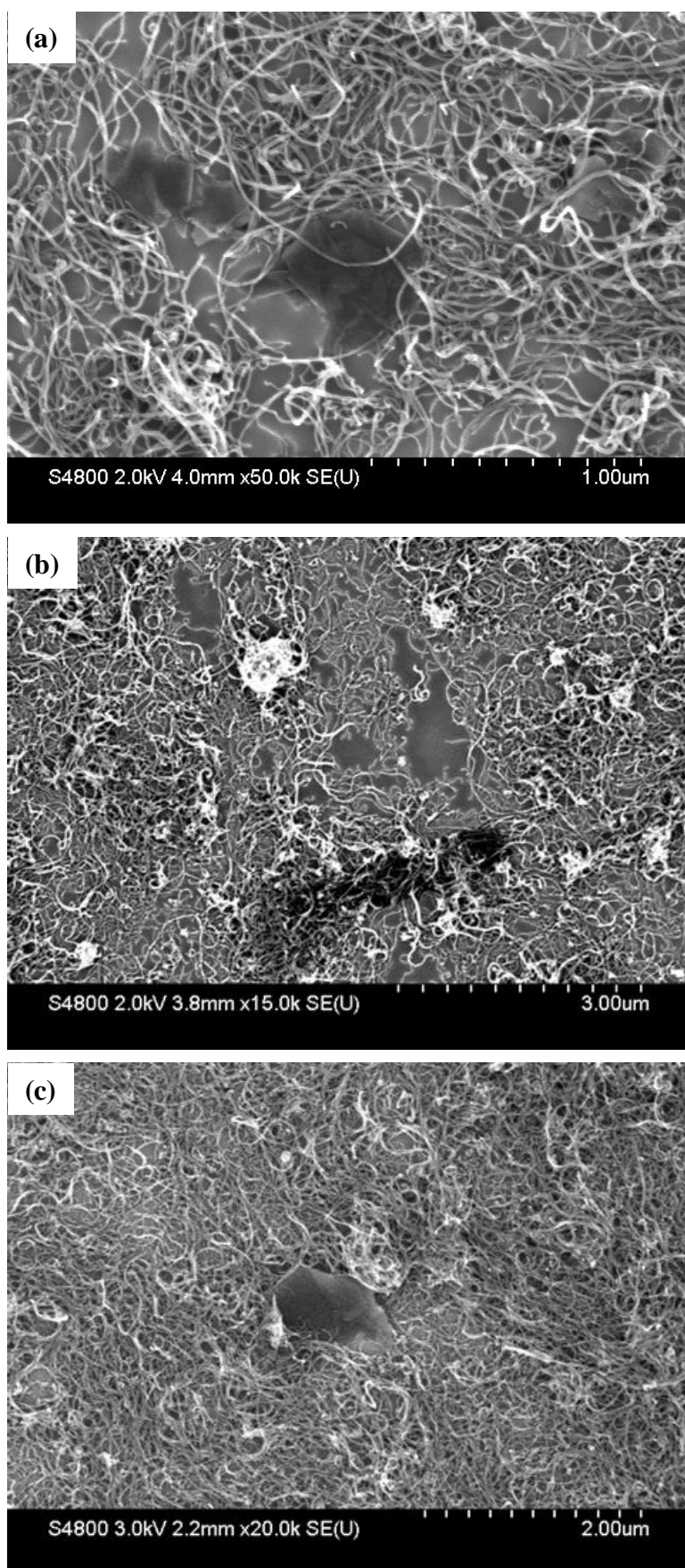
Fig 3.10 SEM images of self-assembled hybrid films with weight ratio of (ME-LOMWNT/ME-LOGr): (a) 25/75, (b) 75/25, and (c) 97/3.

The SEM images of the self-assembled films display crosslinks between MWNTs and graphene sheets, which are supposed to enhance the conductivity of the films. However, the films were not densely packed and were not fully covered with MWNTs and graphene sheets. Indeed, many voids were observed within the films. These voids and the larger distance between the MWNTs and/or graphene sheets within the films limit the electrical pathway of electrons and lead to the decrease in conductivity.

On the other hand, the SEM images of the filtered-films on alumina membrane display an efficient percolating network within the films (Fig 3.11). The filtration approach produced films that were highly entangled and crosslinked with each other.

The different film fabrication methods led to the films with different arrangement of the MWNTs and/or graphene sheets, which leads to different conductive percolated networks. We think this is the main reason for the sheet conductance difference between the interfacial self-assembly method and the filtration method.

(a)

S4800 8.0kV 3.0mm x50.0k SE(U)   1.00um

(b)

S4800 8.0kV 2.9mm x50.0k SE(U)   1.00um

(c)

S4800 8.0kV 2.8mm x60.0k SE(U)   500nm
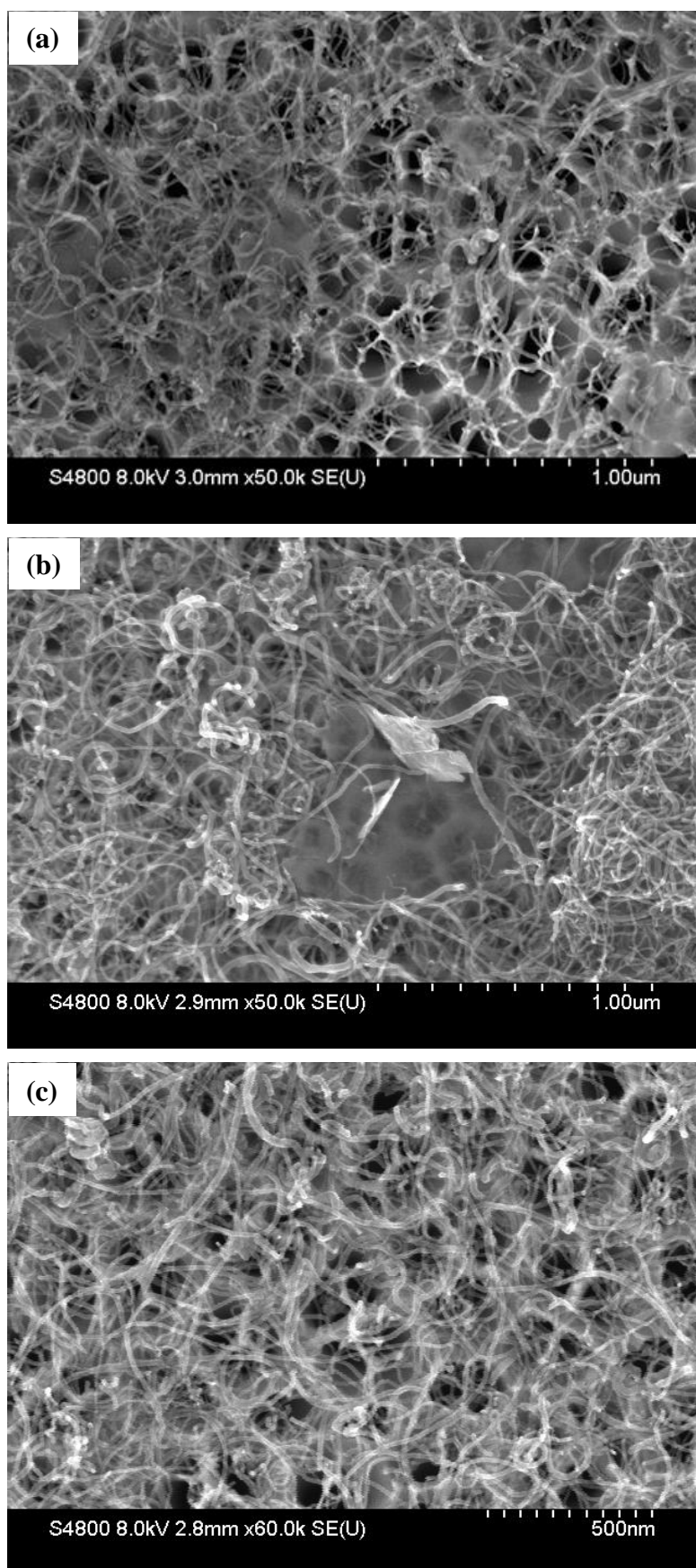
Fig 3.11 SEM images of the hybrid films using filtration with weight ratio of (ME-LOMWNT/ME-LOGr): (a) 25/75, (b) 75/25, and (c) 97/3.

3.3.5 Thermal annealing of the films to further enhance the conductivity of the films

For further improvement on film conductivity, a post-heat treatment was performed on the hybrid films that were formed by filtration method. Sheet resistance was measured before and after the film being transferred onto quartz substrate. Also, sheet resistance was measured after every cycle of the treatment. We found that the sheet resistance of the films prepared by vacuum filtration increased ~26% after the films were transferred from the alumina filtration membrane to quartz substrates. We applied two heating methods to study how thermal annealing treatment can enhance the conductivity of the films.

(a) Traditional heating

Film on	Film Resistance ($\Omega/\square$)					Avg Film Resistance ($\Omega/\square$)
Alumina membrane	158	153	155	158	160	157
Quartz	191	209	201	202	192	199
After Heating Treatment @ 300°C						
Total Heating Time	Film Resistance ($\Omega/\square$)					Avg Film Resistance ($\Omega/\square$)
1	123	126	133	132	121	127
2	119	132	131	127	120	126

Transfer

Table 3.2 Sheet resistance of the wt% 97/3 MF-MWNT/ME-LOGr hybrid film formed using filtration, before and after furnace heating

In an inert environment, achieved by flowing argon gas, the transferred film on quartz was first heated in the tube furnace at 300 °C for an hour, followed by additional 2 hours. The sheet resistance was measured after each cycle of the treatment. Table 3.2 shows that sheet resistance of the film decreased ~36% after first hour of the heat treatment. We

expected further decrease in the sheet resistance with extended period of heat treatment, but additional 2 hours of heating at 300 °C showed no further decrease. The decrease in sheet resistance below 100 °C was mainly due to the evaporation of water molecule; however, the evaporation may occur at higher temperatures for complete evaporation of water molecules.[27] At around 200-300 °C, the oxygen-containing groups of ME-LOMWNTs and ME-LOGr are removed by the prolysis of the hydroxyl, epoxide, and carboxyl groups.[28,29] The removal of these oxygen-containing groups and additional evaporation of water further decreased sheet resistance of the film.
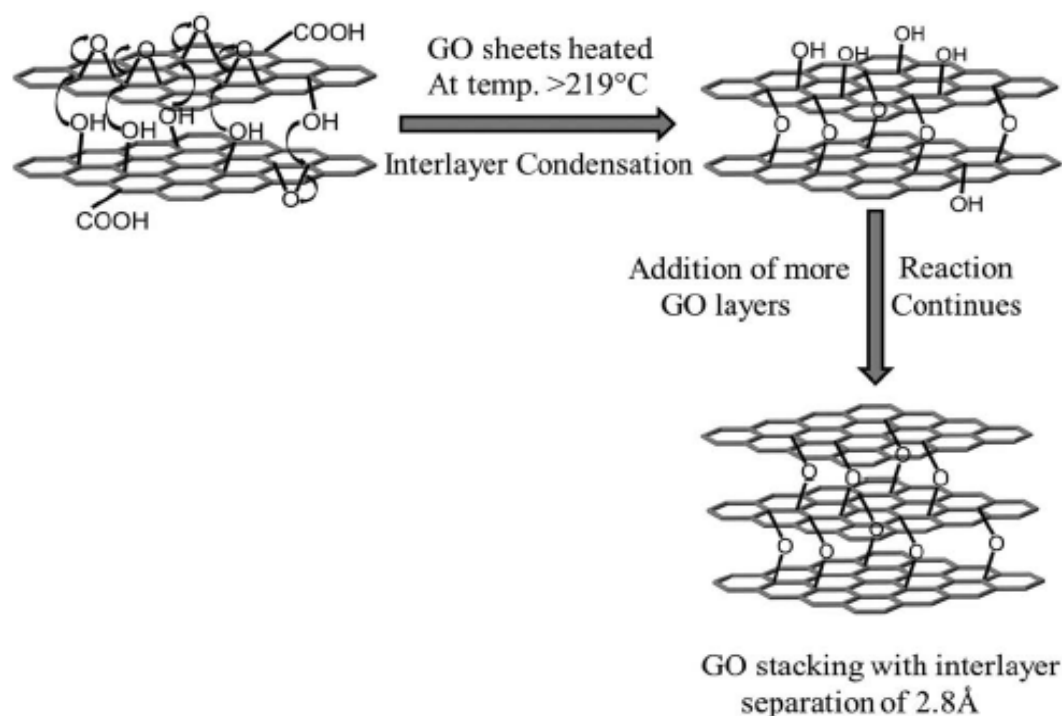

Fig 3.12 Schematic diagram of the mechanism for –C-O-C- bond formation between GO sheets by interlayer condensation. Reproduced from Baskey M.; Saha, S. K. *Adv. Mater.* **2012,** 24, 1590.

A recently work reported by Saha and Baskey demonstrates that a zero indirect gap semiconductor graphene sheets can be chemically synthesized from graphene oxide

(GO) sheets at 219 °C using a thermal annealing process. They attributed their conductivity improvement to the formation of C-O-C bonds between GO sheets with an interlayer separation of 2.8Å (Fig 3.12).[30]

Applying this mechanism, we formulated another explanation for the decrease in sheet resistance after the heat treatment on the film. Although a monolayer of graphene sheet is known to be a zero gap semiconductor, multilayer graphene film is a semimetal.[31] And, the carbon nanotubes have metallic or semiconductor property depended on their structures. As the water molecules within the MWNTs and ME-LOGr evaporate, the gap within and/or between MWNTs and ME-LOGr becomes very close that the C-O-C bonds possibly form within and between them by interlayer and/or intermolecular condensation. However, unexpectedly, the additional heating showed no further decrease in sheet resistance. We believed that the ME-LOMWNTs and ME-LOGr of the film already obtained their optimal crystalline structures in the first hour of heating that the additional heating provided no effect on the sheet resistance of the film.

(b) Microwave heating

Microwave duration (sec)	Power (W)	Sheet resistance (Ω/sq)					Avg sheet resistance (Ω/sq)
		181	171	178	188	180	180
5	200	109	108	109	110	116	110
10	200	89.1	94.9	99.8	97.0	95.0	95.2
10	200	97.1	99.4	104	101	97.2	99.7
20	200	97.5	93.1	102	97.3	97.2	97.4

Table 3.3 Sheet resistance of the wt% 97/3 ME-LOMWNTME-LOGr hybrid film formed using filtration, before and after microwave heating

In a typical heat treatment, traditional heating, such as furnace, is usually being used. Here, we substitute the furnace heating with microwave heating to study the effect

on sheet resistance of the hybrid film. Since the past decades ago, microwave-assisted

chemistry received a great attention in carbon nanostructure chemistry due to the property

of the carbon nanostructures of being strong microwave absorbers.[32,33] Additionally,

microwave-heating has several advantages over conventional heating. A conventional

heating causes a temperature gradient, which leads to a higher temperature of the reaction

vessel than that of actual reaction mixture. On the other hand, microwave heating causes

an inverted temperature gradient, which leads to an instantaneous localized superheating

of the substances so that the actual reaction mixture has a higher temperature than that of

the reaction vessel.[34] A short reaction time is another huge advantage of the microwave

heating over the conventional heating. The carbon nanostructures, including carbon

nanotubes and graphene, are known to be able to strongly absorb microwave energy.[35]

We hope that the advantages of microwave heating can play a role to efficiently reduce

sheet resistance of the film within a short period of time. The microwave heating was

performed at an inert nitrogen gas environment (see apparatus on Fig 3.6 in experimental

procedure 3.2.4b). At microwave power of 200W, several cycles of microwave heating

with different reaction duration were performed on the hybrid film. Sheet resistance of

the film was measured after each cycle of microwave heating treatment (Table 3.3). After

first 5 second of microwave heating, sheet resistance of the film decreased ~37%. As

same as for furnace heating, the decrease in sheet resistance was due to evaporation of

water molecules, pyrolysis of oxygen-containing groups, and possibly reorientation of the

MWNTs and ME-LOGr structures by narrowing the interlayer gap and/or intermolecular

gap. However, a further study is needed to confirm the reorientation of the nanomaterials.

The film showed further decrease, ~13.5%, in sheet resistance, when it was treated for

longer period of time, 10 seconds. However, another cycle of heating showed no significant change in the sheet resistance. Also, increased heat duration did not influence the sheet resistance. From the result of microwave heating, we observed that microwave heating reduces sheet resistance of the film more efficiently, where it showed total ~47% decrease in sheet resistance (from 180 to 95.2 Ω/sq), compared to total ~37% decrease after the furnace heating. Additionally, the efficient decrease was done in shorter period of time than that of furnace heating.

The furnace heating was treated for the self-assembled hybrid films with different weight ratio (ME-LOMWNTs/ME-LOGr: 100/0, 97/3, 75/25, 25/75, and 0/100) to study the effect of weight ratio of ME-LOMWNTs to ME-LOGr on film conductivity during the heat treatment. The same parameters of furnace heating were applied to the self-assembled hybrid films. As expected, all of the films showed dramatic increase in sheet conductance after first hour of furnace heating at 300°C (Table 3.4), by which the conductance of the films increases in a range of from 47 to 160% depending on the weight ratio of ME-LOMWNTs to ME-LOGr. The ME-LOGr-only film showed the largest increase. Along with the sheet resistance measurement, the transmittance of the films was also measured. The results demonstrated the transmittance was not significantly influenced by the annealing treatment, which is very different from previous reports about films formed from heavily oxidized graphene (GO) and carbon nanotubes. With additional 2 hours of heating, the ME-LOGr-only film still showed largest increase in the sheet conductance. For the hybrid films, the film with a higher weight percent of ME-LOGr tended to respond more efficiently to the heating. The hybrid film with 75wt% ME-LOGr also constantly showed increase in the sheet conductance after each heat

treatment, in which the film is predominated by the ME-LOGr. Meanwhile, the films with weight ratio of 97 and 75 wt% ME-LOMWNT showed slight decrease in the sheet conductance. The heat treatment at 500°C for 1 hour led to further increase in sheet conductance of the films, except for the film with weight ratio of 97 wt% ME-LOMWNT.

(%wt) MF-MWNT/ME-LOGr	Avg Film Resistance (KΩ/□)	Avg Film Conductance (S/m)	TRANSMITTANCE (%T)
BEFORE HEAT TREATMENT			
100/0	5.64	1992	60.9
97/3	4.46	2625	59.9
75/25	11.22	1186	75.8
25/75	12.58	1243	81.5
0/100	12.55	906	56.8
AFTER 1HR OF HEAT TREATMENT @ 300°C			
100/0	2.92	3848	62.8
97/3	2.92	4010	64.5
75/25	7.64	1742	67.9
25/75	7.93	1973	71.3
0/100	4.82	2359	54.0
AFTER ADDITIONAL 2 HRS OF HEAT TREATMENT @ 300°C (TOTAL 3HRS)			
100/0	2.75	4086	56.6
97/3	3.05	3839	57.3
75/25	7.74	1719	70.1
25/75	6.99	2238	72.6
0/100	3.59	3167	53.2
AFTER ADDITIONAL 1HR OF HEAT TREATMENT @ 500°C (TOTAL 4HRS)			
100/0	2.70	4161	58.0
97/3	3.16	3705	64.5
75/25	5.69	2339	72.2
25/75	6.41	2441	70.5
0/100	2.18	5215	50.1

Table 3.4 ME-LOMWNT/ME-LOGr hybrid films formed using interfacial self-assembly, before and after furnace heating

During the first hour of heating at 300°C, the sheet conductance of all the films dramatically increased mainly due to evaporation of water molecules. However, the

additional heating provided different result for each film, depended on the weight ratio of the film. The result appeared to be random, but it rather contained interesting features. The MWNT-only and ME-LOGr-only films constantly showed the increase in the sheet conductance after each cycle of heating. Comparing the increase in sheet conductance of the two films, the ME-LOGr-only film had a larger increase, which is consistent with the thermal gravimetric analysis (TGA) results (Fig 3.13).
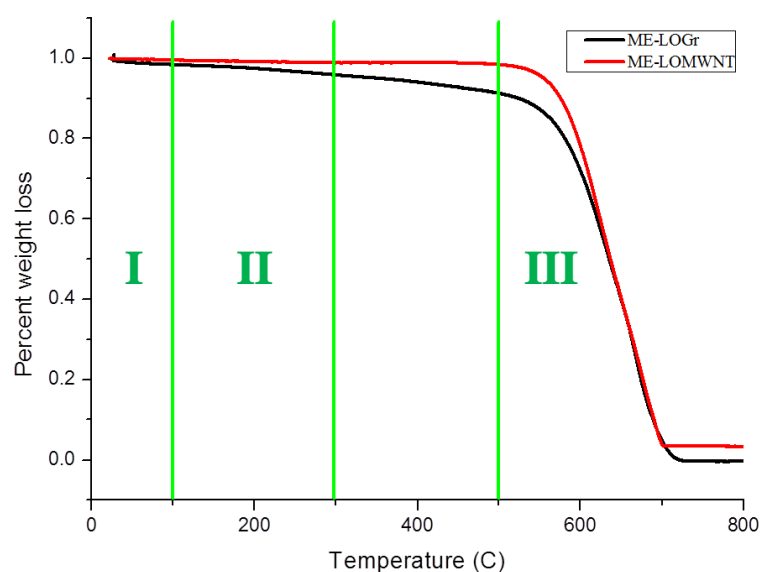
Fig 3.13 TGA curves of ME-LOGr (black) and MWNT (red). Region I: evaporation of water, II: pyrolysis of oxygen-containing groups, III: combustion of carbon

On the TGA results, the mass loss below 100°C has been assigned to desorption of water molecules and the mass loss around 200-300°C has been assigned to pyrolysis of hydroxyl, epoxide, and carboxyl groups.[27,28] TGA for both ME-LOMWNT and ME-LOGr display sharp mass loss above 560 °C, which has been assigned to the combustion of carbon.[29] Around 500 °C, the ME-LOGr showed greater mass loss than the MWNTs, which indicates that ME-LOGr contains more oxygen-containing groups. In other words, with the same heat treatment, ME-LOGr has more hydroxyl, epoxide, and carboxyl

groups to be pyrolysized than ME-LOMWNT. Therefore, the ME-LOGr-only film shows a greater change in the sheet resistance.

3.4   Conclusion

In conclusion, using interfacial self-assembly, we obtained one-atomically thin2D-graphene/1D-MWNTs hybrid films. This new method provides several advantages: (1) it is simple and time-efficient, (2) it assembles highly transparent, conductive thin films, (3) it has capability of producing large quantity of films, and (4) it has some control over the film quality by the amount of ethanol, concentration of solution, and structure of the nanomaterials. We assembled conductive ME-LOMWNT/ME-LOGr hybrid film, with a weight ratio of 97/3 between MWNTs and graphene reached the highest conductivity of 3,630 S/m. Also, our hybrid films were relatively transparent, where their % transmittance ranged from 56.8 to 81.5 %. We found that as the hybrid film contains more MWNT contents, it tends to produce a highly aggregate film. Within this method, we developed a new transfer method, which is facile and fast. Most importantly, it enables us to transfer film to any substrates without any modification. Additionally, we substituted furnace heating with microwave heating for post-heat treatment of the films. While both heat treatments further enhanced the film conductivity, microwave heating effectively enhanced the conductivity of the hybrid films within a shorter time.

References

[1] Kong, B.-S.; Geng, J.; Jung, H.T. *Chem. Commun.*, **2009**, 2174-2176.

[2] Chen, X. D.; Lenhert, S.; Hirtz, M.; Lu, N.; Fuchs, H.; Chi, L. F. *Acc. Chem. Res.,* **2007**, 40, 393.

[3] Tao, A.; Kim, F.; Hess, C.; Goldberger, J.; He, R. R.; Sun, Y. G.; Xia, Y. N.; Yang, P. D. *Nano Lett*., **2003**, 3 229.

[4] Ma, R. Z.; Sasaki, T.; Bando, Y. *J. Am. Chem. Soc*., **2004**, 126, 10382.

[5] Javey, A.; Nam, S. W.; Friedman, R. S.; Yan, H.; Lieber, C. M. *Nano Lett.,* **2007**, 7, 773.

[6] Mihi, A.; Ocana, M.; Miguez, H. *Adv, Mater*., **2006**, 18, 2244.

[7] Shibata, T.; Fukuda, K.; Ebina, Y.; Kogure, T.; Sasaki, T. *Adv. Mater*., **2008**, 20, 231.

[8] Lee, J. H.; Rhee, S. W.; Jung, D.-Y. *Chem. Commun*., **2003**, 2740.

[9] Lee, J. H.; Rhee, S. W.; Jung, D.-Y. *Chem. Commun*., **2004**, 16, 3774.

[10] Lee, J. H.; Rhee, S. W.; Jung, D.-Y. *Chem. Commun*., **2006**, 18, 4740.

[11] Lee, J. H.; Rhee, S. W.; Jung, D.-Y. *Chem. Commun*., **2007**, 129, 3522.

[12] Rabani, E.; Reichman, D. R.; Geissler, P. L.; Brus, L. E. *Nature*. **2003**, 4246, 271.

[13] Bigioni, T. P.; Lin, X.-M.; Nguyen, T. T.; Corwin, E. I.; Witten, T. A.; Jaeger, H. M.; *Nat. Mater*., **2006**, 5, 256.

[14] Musick, M. D.; Keating, C. D.; Lyon, A.; Botsko, S. L.; Holliway, D. J.; McEvoy, T. M.; Richardson, J. N.; Natan, M. J.. *Chem. Mater*., **2000**, 12, 2869.

[15] Kim, B.; Tripp, S. L.; Wei, A. *J. Am. Chem. Soc,*, **2001**, 123, 7955.

[16] Ha, K.; Lee, Y. J.; Lee, H. J.; Yoon, K. B. *Adv. Mater*., **2000**, 12, 1114.

[17] Lee, J. S.; Lim, H.; Ha, K.; Cheong, H.; Yoon, K. B. *Angew. Chem., Int. Ed.* **2006**, 45, 5288.

[18] Hu, L.; Chen, M.; Fang, X.; Wu, L. *Chem. Soc. Rev.,* **2012**, 41, 1350-1362.

[19] Torsten, T.; Wang, J.; Tolbert, S. H.; Dunn, B. *Nat.* Mater., **2010**, 9, 146,

[20] Yang, F.; Forreset, S. R. *Adv. Mater*., **2006**, 18, 2018.

[21] Liu, P.; Liu, L.; Wei, Y.; Liu, K.; Chen, C.; Jiang, K. L.; Li, Q. Q.; Fan, S. S. *Adv. Mater.,* **2009**, 21, 3563.

[22] Dwyer, C. O.; Szachowicz, M.; Visimberga, G.; Lavayen, V.; Newcomb, S. B.; Torres, C. M. S. *Nat. Nanotechnol*., **2009**, 4, 239.

[23] Gudarizi, M. M.; Sharif, F. *Soft Matter*, **2011**, 7, 3432-3440.

[24] Reincke, F.; Hickey, S. G.; Kegel, W. K.; Vanmaekelbergh, D. *Angew. Chem.* **2004**, 116, 464-468.

[25] Matsui, J.; Yamamoto, K.; Inokuma, N.; Orikasa, H.; Kyotani, T.; Miyashita, T. *J. Mater. Chem.,* **2007**, 17, 3806-3811.

[26] Huang, Z.-D.; Zhang, B.; Oh, S.-W.; Zheng, Q.-B.; Lin, X.-Y.; Yousefi, N.; Kim, J.-Y. *J. Mater. Chem.* **2012**, 22, 3591-3599.

[27] Bagri, A.; Mattevi, C.; Acik, M.; Chabal, Y. J.; Chhowalla, M.; Shenoy, V. B. *Nature Chem.* **2010**, 2, 581.

[28] Kittaka, S.; Fukuhara, N.; Sumida, H. *J. Chem. Soc., Faraday Trans.***1993**, 89, 3827.

[29] Boehm, H. P. *Carbon* **2002**, 40, 145.

[30] Baskey, M.; Saha, S.K. *Adv. Mater.* **2012**, 24, 1589-1593.

[31] S.M.-M. Dubois, Z. Zanolli, X. Declerck, and J.-C. Charlier. Eur. Phys. J. B. **2009**, 1-22.

[32] Imholt, T.J.; Kyke, C.A.; Hasslacher, B.; Perez, J.M.; Price, D.W.; Roberts, J.A.; Scott, J.B.; Wadhawan, A.; Ye, Z.; Tour, J.M. *Chem. Mater.* **2003**, 15, 3969-3970.

[33] Vazquez, E.; Prato, M. *ACS Nano* **2009,** 3, 3819-3824.

[34] Kappe, C.O.; Dallinger, C.; Murphree, S.S. Practical Microwave Synthesis for Organic Chemists: Strategies, Instruments, and Protocols. Wiley-VCH, Weinheim, **2009**.

[35] Lin, W; Moon, K.-S.; Zhang, S.; Ding, Y.; Shang, J.; Chen, M.; Wong, C.-P. *Am. Chem. Soc.* **2010**. 4(3), 1716-1717.

Curriculum Vitae

Min Jeong
Email: minj614@gmail.com

Date and Place of Birth: June 14, 1986. Seoul, South Korea.

EDUCATIONS

Rutgers-Newark University   *Newark, NJ*
- Master of Science Degree in Chemistry   Jan. 2010-May 2012
- Supervisor: Professor Huixin He

University of Southern California   *Los Angeles, CA*
- Bachelor of Science Degree in Chemistry   Sept. 2004-May 2008
- Supervisor: Professor Kyung W. Jung

PUBLICATIONS

- Expeditious Enyne Construction form Alkynes via Oxidative Pd(II)-Catalyzed Heck-Type Coupling. Victor Hadi, Kyung Soo Yoo, **Min Jeong**, Kyung Woon Jung. *Tetrahedron Lett.* **2009**, 50(20), 2370-2373.
- Microwave- and Nitronium Ion-Enabled Rapid and Direct Production of Highly Conductive Low-Oxygen Graphene. Pui Lam Chiu, Daniel D. T. Mastrogiovanni, Dongguang Wei, Cassandre Louis, **Min Jeong**, Guo Yu, Peter saad, Carol R. Flach, Richard Mendelsohn, Eric Garfunkel, and Huixin He. *J. Am. Chem. Soc.,* **2012**, 134(13), 5850-5856.

WORK EXPERIENCES

Huntington Medical Research Institutes   *Pasadena, CA*
- Summer Intern in Neural Engineering Department   June 2011–August 2011
- Supervisor: Dr. Victor Pikov

Good Samaritan Hospital   *Los Angeles, CA*
- Volunteer   Summer 2007